Regulation of adaptive growth decisions via phosphorylation of the TRAPPII complex in Arabidopsis.

Christian Wiese[1,2], Miriam Abele[2,3], Benjamin Al[2], Melina Altmann[4], Alexander Steiner[2], Nils Kalbfuß[2], Alexander Strohmayr[1,2], Raksha Ravikumar[2], Chan Ho Park[5], Barbara Brunschweiger[2], Chen Meng[3], Eva Facher[6], David W. Ehrhardt[5], Pascal Falter-Braun[4], Zhiyong Wang[5], Christina Ludwig[3] and Farhah F. Assaad[1,2,*]

[1]Biotechnology of Natural Products, TUM School of Life Sciences, Technical University of Munich, 85354 Freising, Germany.
[2]Botany, TUM School of Life Sciences, Technical University of Munich, 85354 Freising, Germany.
[3]Bavarian Center for Biomolecular Mass Spectrometry (BayBioMS), TUM School of Life Sciences, Technical University of Munich, 85354 Freising, Germany.
[4]Institute of Network Biology (INET), Helmholtz Center Munich, German Research Center for Environmental Health, 85764 Neuherberg, Germany.
[5]Department of Plant Biology, Carnegie Institution for Science, Stanford, 94305 California, USA.
[6]Systematic Botany and Mycology, Faculty of Biology, Ludwig-Maximilians-Universität (LMU) München, 82152 Planegg-Martinsried, Germany.
* Corresponding author. Email: farhah.assaad@tum.de

ABSTRACT

Plants often adapt to adverse or stress conditions via differential growth. The trans-Golgi Network (TGN) has been implicated in stress responses, but it is not clear in what capacity it mediates adaptive growth decisions. In this study, we assess the role of the TGN in stress responses by exploring the interactome of the Transport Protein Particle II (TRAPPII) complex, required for TGN structure and function. Together with yeast-two-hybrid screens, this identified shaggy-like kinases (GSK3/AtSKs) as TRAPPII interactors. Kinase assays and pharmacological inhibition provided *in vitro* and *in vivo* evidence that AtSKs target the TRAPPII-specific subunit AtTRS120. We identified three GSK3/AtSK phosphorylation sites in AtTRS120. These sites were mutated, and the resulting AtTRS120 phosphovariants subjected to a variety of single and multiple stress conditions. The non-phosphorylatable TRS120 mutant exhibited enhanced adaptation to multiple stress conditions and to osmotic stress whereas the phosphomimetic version was less resilient. This suggests that

the TRAPPII phosphostatus mediates adaptive responses to abiotic stress factors. AtSKs are multitaskers that integrate a broad range of signals. Similarly, the TRAPPII interactome is vast and considerably enriched in signaling components. An AtSK-TRAPPII interaction would integrate all levels of cellular organization and instruct the TGN, a central and highly discriminate cellular hub, as to how to mobilize and allocate resources to optimize growth and survival under limiting or adverse conditions.

Key words: TRAPPII, GSK3/shaggy-like kinases, BRASSINOSTEROID INSENSITIVE 2 (BIN2), decision-making, growth trade-offs, light responses, water stress, adaptation, osmotic stress, additive stress, TGN, Arabidopsis

INTRODUCTION

Plant responses to environmental stimuli involve diverse forms of growth or movement. The slow, cyclic movement of shoots and stems helps climbing plants such as vines find supportive structures, and stem growth or tendrils are then used to wrap around and cling to such structures (Darwin, 2009). Leaf movements linked to the circadian rhythm enable plants to maximize their exposure to sunlight (McClung, 2006). Tropisms are additional examples of movement in plants: the shoot bends towards directional light, whereas the root bends away from the light. In addition to phototropism, plants have tropic responses to a range of stimuli including moisture, fluctuations in temperature, gravity, touch and other mechanical cues (Garzón & Keijzer, 2011). Darwin argues that the movements of plants are driven by growth and the need to access resources, such as sunlight and water (Darwin, 2009). Leaf movements are driven either by specialized motor cells or by the differential expansion of cells on the adaxial and abaxial sides of petioles (Whippo & Hangarter, 2009; Polko *et al*, 2012; Rauf *et al*, 2013). Gyrations, revolutions and tropisms require some form of differential growth or bending at the organ level. Bending is achieved when one side of an organ grows more rapidly than the opposing side. This differential growth is a result, at least in part, of the differential sorting of PIN-FORMED (PIN) auxin transporters, resulting in the unequal distribution of auxin, a morphogen, at opposing sides of a cell (Friml *et al*, 2002; Ding *et al*, 2011). It follows that differential growth responses such as bending require differential sorting decisions. How environmental stimuli are translated into sorting decisions remains largely unclear.

The sorting of PIN transporters has been shown to require trans-Golgi network (TGN) function. Indeed, disruption of TGN function by mutation results in the ectopic distribution of PIN or AUX proteins (Naramoto *et al*, 2014; Qi *et al*, 2011; Rybak *et al*, 2014; Ravikumar *et al*, 2018). The TGN plays a key role not only in the sorting of macromolecules, but also in exocytosis and endocytosis. In addition, the TGN performs specialized functions such as cytokinesis, cell differentiation, the establishment of cell polarity, and anisotropic growth (Gendre *et al*, 2015; Ravikumar *et al*, 2017). As an early endosome, the plant TGN is a central hub in the flow of information to and from the plant cell surface (Uemura, 2016). The plant TGN has been implicated in responses to abiotic stimuli such as drought, heat, salt stress and osmotic stress and to biotic stimuli such as fungal attack (Rosquete & Drakakaki, 2018). Studies on the role of the TGN in stress responses have been carried out predominantly with core trafficking components such as Rab-GTPases, tethering factors, and Q-SNAREs, required for membrane tethering, docking and fusion (Rosquete & Drakakaki, 2018; Ravikumar *et al*, 2017). Trafficking mutants typically exhibit root growth defects and/or hypersensitivity to abiotic cues such as salt stress, osmotic stress, drought or heat (Asaoka *et al*, 2013; Kim & Bassham, 2011; Lee *et al*, 2006; Rosquete *et al*, 2019; Uemura *et al*, 2012; Wang *et al*, 2011; Zhu *et al*, 2002). However, whether trafficking mutants have primary defects in growth with secondary consequences in stress responses, or whether the primary defects lie in an ability to respond to stress factors remains unclear. More broadly, in the context of stress responses the question pertains as to whether the TGN is involved in decision-making processes *per se*, or merely in the execution of adaptive growth decisions.

As regards decision-making processes, there is a growing body of evidence to suggest that plants have the ability to learn, to process information, to communicate, to reach decisions, and in general to exhibit behavior that could be considered cognitive (reviewed in Severino, 2021). For instance, researchers have found that plants can "remember" a previous exposure to stress and respond more effectively to that same stressor in the future (Galviz *et al*, 2020). Plants can allocate resources such as nutrients to different parts of the plant in a way that maximizes their overall fitness (Ericsson, 1995). Plants can also reach adaptive decisions in response to their environment; for example, some plants can detect the presence of a nearby competitor and adjust their growth patterns to optimize access to resources (Silvertown & Gordon, 1989). There is still controversy in the scientific community over the appropriate use of terms to describe the above observations. Some scientists argue that the behaviors observed in plants are better explained by simpler mechanisms, such as chemical or mechanical responses, rather than true cognitive processes. To avoid such controversy, Severino (2021) makes the case for experimental

102 approaches. A recent experimental approach for the study of decision-making processes in
103 germinating seedlings has incorporated two tools used in decision theory: the use of a limited
104 budget and of conflict-of interest scenarios (Kalbfuß *et al*, 2022). A limited budget was achieved
105 by germination in the dark and a conflict-of-interest by the simultaneous withdrawal of light and
106 water; as a binary readout for responses to these additive stress conditions, tradeoffs in hypocotyl
107 versus root growth were monitored (Kalbfuß *et al*, 2022). By emphasizing growth trade-offs, the
108 experimental approach developed by Kalbfuß *et al* (2022) is aligned with the definition of decision-
109 making as entailing an appraisal of the advantages and disadvantages of various courses of action
110 (Karban & Orrock, 2018). While Kalbfuß *et al* (2022) address decision-making at a cellular level,
111 the literature on plant decision-making has, to our knowledge, not included considerations about
112 the possible role of the TGN.
113
114 In order to understand the role of the TGN in adaptive or stress responses, it would be important
115 to deploy a battery of gene products not only broadly associated with or localized to the TGN, but
116 also intrinsic to TGN structure and function. Two such proteins or complexes are ECHIDNA and
117 the Transport Protein Particle II (TRAPPII) tethering complex. ECHIDNA was identified as an
118 upregulated transcript in elongating cells (Gendre *et al*, 2011). *echidna* mutants have defects in
119 cell elongation and hook formation as well as in pollen formation, release and fertilization (Boutté
120 *et al*, 2013; Fan *et al*, 2014; Gendre *et al*, 2011, 2013; Ravikumar *et al*, 2018). The Arabidopsis
121 TRAPPII (AtTRAPPII) complex was identified by mutation in screens for seedlings with aberrant
122 morphogenesis or cytokinesis defects (Söllner *et al*, 2002; Thellmann *et al*, 2010; Jaber *et al*,
123 2010). AtTRAPPII consists of six shared core subunits and three TRAPPII-specific subunits
124 (AtTRS120, CLUB/AtTRS130 and TRIPP; Garcia *et al*, 2020; Kalde *et al*, 2019). With the
125 exception of the plant-specific TRIPP subunit, AtTRAPPII most resembles fungal and metazoan
126 TRAPPII complexes (Garcia *et al*, 2020; Kalde *et al*, 2019; Pinar *et al*, 2019). We have previously
127 shown that ECHIDNA and TRAPPII have overlapping yet distinct functions at the TGN (Ravikumar
128 *et al*, 2018). ECHIDNA is primarily required for the genesis of secretory vesicles and, as a
129 consequence, for cell expansion (Boutté *et al*, 2013; Gendre *et al*, 2013; McFarlane *et al*, 2013).
130 AtTRAPPII plays a role not only in basal TGN functions - exocytosis, endocytosis, protein sorting
131 - but also in more specialized TGN functions such as cytokinesis and the establishment of cell
132 polarity (Ravikumar *et al*, 2018). Whether or not AtTRAPPII plays a role in responses to abiotic
133 cues such as osmotic or drought stress remains to be determined.
134

135 In this study, we focus on the TRAPPII complex as a starting point as it is required for all aspects
136 of TGN function, including the sorting of proteins such as PINs to distinct membrane domains (Qi
137 *et al*, 2011; Ravikumar *et al*, 2018). We first explored the TRAPPII interactome and also surveyed
138 dynamic or conditional interactions. Together with yeast-two-hybrid screens, this identified
139 shaggy-like kinases such as AtSK21/BIN2 as TRAPPII interactors. We corroborated this finding
140 with *in vitro* kinases assays and pharmacological inhibition *in vivo*. Shaggy-like kinases are multi-
141 taskers that integrate a vast number of biotic and abiotic cues (Lv & Li, 2020; Planas-Riverola *et*
142 *al*, 2019; Youn & Kim, 2015; Li *et al*, 2021; Song *et al*, 2023). AtSK21/BIN2 has recently been
143 implicated in decision-making in the Arabidopsis seedling (Kalbfuß *et al*, 2022). We explore the
144 meaning of the AtSK-TRAPPII interaction using a variety of assays to monitor stress responses
145 and differential growth decisions.
146
147
148 **RESULTS**
149 **The TRAPPII interactome contains a large number of signaling components**
150 To gain insight into TGN function, we used the TRAPPII interactome as a starting point. We first
151 carried out a gene ontology (GO) term enrichment analysis (Fig. 1A; Kalde *et al*, 2019; Rybak *et*
152 *al*, 2014). The TRAPPII interactome was significantly enriched in proteins involved in (i) cell
153 division, (ii) the organization of the cytoskeleton or of cellular or sub-cellular compartments and
154 (iii) in trafficking or transport (Fig. 1A). This is consistent with known *trappii* phenotypes such as
155 defects in microtubule organization, in cytokinesis and in the structure and function of the TGN
156 (Jaber *et al*, 2010; Qi *et al*, 2011; Rybak *et al*, 2014; Steiner *et al*, 2016; Ravikumar *et al*, 2018).
157 GO terms describing developmental processes were also scored, and this is equally unsurprising
158 in light of *trappii* defects in root growth, in root hair morphogenesis, in transmission through the
159 pollen and in vein development (Fig. 1A; Jaber *et al*, 2010; Naramoto *et al*, 2014; Söllner *et al*,
160 2002; Thellmann *et al*, 2010). GO terms describing transcription, translation and post-translational
161 protein modifications such as deneddylation, acetylation and dephosphorylation were also
162 prominently enriched (Fig. 1A). Interestingly, a large number of significantly enriched GO
163 categories describe responses to abiotic cues such as light, cold, metal ions or chemicals
164 (grouped under “response to stimulus” in Fig. 1A).
165 To further explore a possible implication of the TRAPPII complex in signaling, we surveyed the
166 dynamic interactome, by which we refer to interactors perceived under one environmental
167 condition (for example in the light) but not in another (for example in the dark). By these criteria,
168 brassinosteroid signaling components were significantly enriched ($p = 0.016$); this category

169 encompasses 11 proteins, of which 9 were detected in CLUB-GFP immunoprecipitates from light-
170 grown influorescences (Fig. S1; Table S2). Among these were the TOR kinase and a family of
171 shaggy-like kinases (AtSKs; Fig. S1; Table S2). TOR and AtSKs are highly significant interactors
172 in the TRAPPII interactome (Fig. S1; Fig. 1B). They show a fold enrichment that is lower than seen
173 for components of the TRAPPII complex, but similar to that seen for validated interactors such as
174 RabA2a and MAP65, expected to form more transient associations (Fig. S1; Fig. 1B; Kalde *et al*,
175 2019; Steiner *et al*, 2016). We then used yeast two-hybrid (Y2H) to probe for binary interactions
176 between TRAPPII and signaling components identified in the IP-MS. Y2H was carried out with
177 TRAPPII subunits and truncations thereof (Kalde *et al*, 2019; Steiner *et al*, 2016; Garcia *et al*,
178 2020). In a large scale Y2H screen including 2400 pair-wise tests, an interaction was detected
179 between a TRS120$^{499-1187}$ truncation (referred to below as TRS120-T2) and the shaggy-like kinase
180 BIN2 (AtSK21; Fig. 1C). BIN2 interacted specifically with AtTRS120 and not with other tested
181 TRAPPII subunits (Fig. 1C). Furthermore, we did not detect any other TRAPPII-kinase interactions
182 in our pairwise Y2H assays.
183
184 **The TRAPPII complex is a target of shaggy-like kinases**
185 To assess whether the TRAPPII complex is a target of AtSK/GSK3 kinases, we first looked for the
186 presence of phosphopeptides in co-immunoprecipitates. To this end, we immunoprecipitated two
187 TRAPPII-specific subunits, AtTRS120 and CLUB/AtTRS130, and looked for phosphopeptides via
188 mass spectrometry. This provided ample *in vivo* evidence for TRAPPII AtTRS120 phosphorylation
189 at AtSK/GSK3 sites (Fig. S2). Furthermore, shaggy-like kinases were detected in IP-MS not only
190 with the TRAPPII-specific subunit CLUB/AtTRS130 (Fig. 1B; Fig. S1) but also with the TRAPPII-
191 specific subunit AtTRS120 (Fig. S3). The Arabidopsis genome encodes ten shaggy-like kinases
192 (AtSKs), which are classified into four clades (Fig. S3A).
193 The TRS120-T2 truncation contains the GSK3 sites we had found to be phosphorylated *in vivo*
194 (Fig. S2; see yellow highlights in Fig. 2B). Our nomenclature for these sites is α, β and γ, which is
195 short for TRS120-S922:S923 (α), TRS120-S971:S973:S974:S975 (β) and TRS120-S1165 (γ; Fig.
196 2B). Alpha-fold structural predictions (Varadi *et al*, 2022; Jumper *et al*, 2021) show that the three
197 sites reside in unstructured, flexible and accessible regions of the AtTRS120 protein, as is
198 observed in the majority of modified amino acid residues (Fig. 2C-D; Jiménez *et al*, 2007). These
199 reside in the plant-specific moiety of AtTRS120 and are embedded in plant-specific sequences at
200 the dimer interface (see green shading in Fig. 2A; Fig. 2E). To study the three sites, we generated
201 site directed mutations in TRS120-T2, mutating the serine (S) and threonine (T) residues (depicted
202 in red in Fig. 2B) to non-phosphorylatable alanine (A) residues, or to aspartate (D) to mimic

203 constitutive phosphorylation. In the case of the TRS120-Sβ site, for example, we designate these
204 variants as TRS120-SβA or TRS120-SβD (Fig. 2F; Fig. 3A). The point mutations were introduced
205 into cDNA sequences for expression in yeast and bacteria.
206
207 The IP-MS and Y2H interactions were validated with *in vitro* kinase assays, performed with a
208 phosphorus radioisotope (Fig. 3A; Fig. S4). Further, the phosphorylation was confirmed with
209 mass-spectrometry using non-radioactive assays. The mass-spectrometry results showed that the
210 AtTRS120 α, β, and γ sites phosphorylated *in vivo* (Fig. S2; IP-MS on seedlings using TRS120-
211 GFP as bait) were phosphorylated by AtSKs *in vitro* (Fig. 3B, 3C). Kinase assays performed with
212 varying kinase concentrations (but constant substrate concentrations) showed that the
213 phosphorylation events were time and/or concentration dependent (Fig. 3C). AtTRS120 was a
214 substrate of AtSKs in clades I-III; we did not detect phosphorylation of AtTRS120 with a clade IV
215 AtSK *in vitro* (Fig. 3C). All AtSKs that targeted AtTRS120 had a marked and consistent preference
216 for the TRS120-γ (S1165) site (Fig. 3C). *In vivo*, IP-MS performed on seedlings treated with the
217 AtSK inhibitor bikinin showed a reduced extent of phosphorylation of the TRS120-γ peptide (Fig.
218 S5), which is consistent with the *in vitro* data (Fig. 3C). In Y2H screens, the BIN2-TRS120
219 interaction, but not TRAPPII complex interactions, was almost abolished when all three sites were
220 mutated from S to D (TRS120-SαβγD; Fig. 2F). In summary, several lines of *in vitro* (Y2H, kinase
221 assays) and *in vivo* (IP-MS, pharmacological inhibition) evidence support the conclusion that the
222 TRAPPII subunit AtTRS120 is a substrate of shaggy-like kinases.
223
224 **BIN2 and TRAPPII are required for differential growth decisions under additive stress**
225 As TRAPPII is a BIN2 substrate, a question is whether *bin2* and *trappii* mutants have related
226 phenotypes. We were not able to detect cytokinesis or protein sorting defects, characteristic of
227 *trappii,* in semi-dominant *bin2-1* alleles (Fig. S6). We have recently shown that BIN2 is required
228 for hypocotyl versus root tradeoffs in the germinating seedling under additive stress conditions
229 involving the simultaneous withdrawal of both light and water (Kalbfuß *et al*, 2022). Water stress
230 in the dark is a “conflict of interest” scenario in which hypocotyl and root growth have competing
231 interests (Kalbfuß *et al*, 2022). Kalbfuß *et al*, 2022 defined decision mutants as ones that had
232 either insignificant responses ($P > 0.05$), or consistently wrong growth responses as compared to
233 the wild-type ($P < 0.05$ but for an opposite growth phenotype, as depicted by red asterisks in Fig.
234 4B, 4C, 4D; Kalbfuß *et al*, 2022). Under additive stress, *trappii* null mutants failed to adjust their
235 hypocotyl length along the same line as the wild-type (red asterisk in Fig. 4C, 4D; see Fig. 4F for
236 a direct comparison to the wild-type and for the distribution of datapoints). In particular, *trappii*

237 *trs120-4* mutants had non-significant hypocotyl/root ratio responses to water withdrawal in the
238 dark (Fig. 4D). Due to some variability between PEG plates and experiments, we normalized each
239 mutant line to its corresponding wild-type ecotype on the same (PEG) plate in the same
240 experiment. To this end, the response to water stress in the dark was represented as a normalized
241 response quotient (RQ). The RQ is an indication of how much the mutant deviates from the
242 corresponding wild-type and enables us to summarize replicate experiments (see methods for
243 further detail; the RQ_{ratio} is depicted in Fig. 4G and the $RQ_{hypocotyl}$ and RQ_{root} in Fig. S7). We reason
244 that mutants unable to integrate environmental cues might have a "confused phenotype" under
245 multiple stress conditions. The read out for a "confused phenotype" would translate into erratic
246 (i.e. highly variable) hypocotyl versus root lengths. This high variance would, in turn, translate into
247 a low signal-to-noise ratio, and this can be seen as a high *P*-value. We, therefore, plotted the
248 median *P*-values against the normalized response quotients (referred to as volcano plots; mean
249 RQ_{ratio} in Fig. 4H). Wild-type ecotypes invariably had low *P*-values < 10^{-10} (grey shading on the red
250 line in Fig. 4H, green arrow). Mutants with high *P*-values and low response quotients would be
251 considered "confused" and these would map in the lower left quadrant of the RQ_{ratio} volcano plot
252 (see peach shading in Fig. 4H). *bin2* higher order null alleles and *trs120-4* mutants cluster together
253 in the lower left region of the volcano plot (see peach shading in Fig. 4H); both qualify as decision
254 mutants (Fig. 4B, 4D, 4F-H; Kalbfuß *et al*, 2022).
255
256 A question that arises is whether *trappii* mutants are impaired in differential growth decisions as a
257 secondary consequence of primary defects in cytokinesis (Jaber *et al*, 2010; Rybak *et al*, 2014;
258 Thellmann *et al*, 2010). The etiolation response was severely attenuated in *trappii* mutants, but
259 nonetheless highly significant (P < 0.00001; Fig. S8C, S8D, S8F-G). Similarly, an attenuated but
260 clear etiolation response has been shown for other cytokinesis-defective mutants including *keule*
261 and *knolle* (Assaad *et al*, 2001). This shows that, despite a severe impairment in cell division,
262 cytokinesis-defective mutants are nonetheless capable of differential growth. In addition to their
263 cytokinesis defect, *trappii* mutants are impaired in TGN function (Ravikumar *et al*, 2018). We,
264 therefore, compared *trappii* mutants to *echidna* mutants, severely impaired in TGN structure and
265 function (Boutté *et al*, 2013; Gendre *et al*, 2013; McFarlane *et al*, 2013). Both *echidna* and *trappii*
266 mutants exhibited a severe impairment in root elongation in the light (Fig. S8 C-E). In contrast to
267 *trappii*, however, *echidna* mutants had highly significant responses to additive stress that
268 resembled the wild-type in all respects (Fig. 4E, 4G, 4H). The *trappii* decision phenotype was
269 shared neither by *echidna* mutants, nor by higher order null mutants impaired in the perception of
270 light or water stress (Fig. 4G, 4H). In conclusion, a comparison to other cytokinesis-defective or

271 TGN mutants suggests that neither cytokinesis defects nor TGN malfunction suffice to explain the
272 *trappii trs120-4* decision phenotype.
273 Cellular growth parameters in *trappii* were assessed by scanning electron microscopy (SEM) in
274 the hypocotyl and by confocal microscopy in root tips. In wild-type hypocotyls, both organ length
275 and cell length decrease in response to water stress in the dark (Fig. 4A; Fig. 5A). In contrast, in
276 *trappii* mutants, organ and cell length significantly increased (red asterisks in Fig. 4C, 4D and in
277 Fig. 5B, 5C highlight a phenotype consistently opposite to the wild-type). This was more
278 pronounced in *trs120-4* (1.71-fold increase; Fig. 5C) than in *club-2* (1.46-fold increase; Fig. 5B)
279 whereas the wild-type Col-0 showed a 0.55-fold decrease in cell length. In root tips, we monitored
280 meristem properties and cell length along single cortical cell files as a function of distance from
281 the quiescent center. In the wild-type, meristem size was large in the light, intermediate in the dark
282 and shortest under water stress in the dark (darkW; Fig. 6A-C). In contrast, meristem size in
283 *trs120-4* remained constant under the three environmental conditions tested (Fig. 6E-G). We have
284 recently shown that root growth in response to water stress in the dark is due to a combination of
285 cell division and rapid exit from the meristem (Kalbfuß *et al*, 2022). An early exit from the meristem
286 can be visualized as cell elongation in cells close to the quiescent center. This was observed
287 under dark and darkW conditions in the wild-type (green arrows in Fig. 6D) but not in the *trappii*
288 mutant *trs120-4* (magenta arrows in Fig. 6H). While the curves differed under the different
289 environmental conditions in the wild-type (Fig. 6D), these were fairly similar regardless of the
290 environmental cue in *trs120-4* (magenta arrows in Fig. 6H; note that the grey shading, which
291 designates the 95% confidence interval, overlaps). We conclude that, at a cellular level, *trappii*
292 *trs120-4* mutants are unable to differentially regulate their growth parameters (Fig. 5, Fig. 6). This
293 would suffice to explain the growth defects we observed at the organ level (Fig. 4). In summary,
294 *bin2* and *trappii* alleles have related phenotypes w.r.t. an inability to differentially regulate cell
295 growth in both the hypocotyl and root tip in response to additive stress (Figs. 4-6; cf. Kalbfuß *et*
296 *al*, 2022).
297
298 **AtTRS120 phosphovariants are functional**
299 To assess the impact of phosphorylation status on intracellular localization, targeted point
300 mutations at the TRS120 AtSK sites (Fig. 2B) were introduced into genomic sequences capable
301 of rescuing the *trs120-4* mutant phenotype (Rybak *et al*, 2014). The TRS120 constructs were
302 fused to a C-terminal GFP tag and we refer to the ensuing site-directed mutants as TRS120
303 phosphovariants. The constructs were expressed and capable of rescuing the null *trs120-4* allele
304 in the T1 and T2 generations (Fig. S9A, S9B); upon further propagation, however, the GFP signal

305 (but not the ability to rescue the mutant phenotype) was lost and signs of silencing were evident
306 (Fig. S9C, S9D). The wild-type TRAPPII complex resides in the cytosol, at the TGN and at the cell
307 plate (Fig. S10A; Naramoto *et al*, 2014; Qi *et al*, 2011; Ravikumar *et al*, 2018; Rybak *et al*, 2014).
308 Phosphovariants had a similar appearance, but the phosphomimetic S to D variant tended to be
309 mostly membrane associated, with almost no detectable cytosolic signal (Fig. S10).
310

311 **TRS120-SαβγA and TRS120-SαβγD have opposite effects on seed germination under**
312 **osmotic stress**

313 We first analyzed the impact of osmotic stress on the germination frequencies of TRS120
314 phosphovariants. Different TRS120-SαβγA and TRS120-SαβγD primary transformants were
315 plated on media containing 0, 200, or 400 mM mannitol (Fig. 7A-C). As compared with the control
316 (Col-0), the TRS120-SαβγA phosphovariant had higher seed germination rates on mannitol: on
317 day 4 we observed 70% germination in TRS120-SαβγA versus 35% germination for the control
318 on 400 mM mannitol as an osmotic agent (Fig. 7C). In this respect, TRS120-SαβγA was similar to
319 the ABA deficient mutant *aba2-1* on mannitol (Fig. 7C). In contrast, the TRS120-SαβγD
320 phosphovariant exhibited delayed and reduced germination, with lower maximal germination
321 rates, even in the absence of mannitol (Fig. 7A-C). Indeed, on 400 mM mannitol TRS120-SαβγD
322 mutants reached a maximal germination rate of 60% compared to 90% for the wild-type. With
323 respect to its delay in germination, TRS120-SαβγD was similar to the ABA coreceptor higher order
324 mutant *hab1-1 abi1-2 pp2ca-1* on mannitol (Fig. 7C). In summary, the non-phosphorylatable
325 TRS120-SαβγA mutations enhanced whereas the phosphomimetic TRS120-SαβγD mutations
326 reduced germination on mannitol.
327

328 **TRS120 phosphorylation status affects hypocotyl versus root trade-offs under additive**
329 **stress conditions**

330 In light of the decision phenotypes of *bin2* and *trappii* mutants and of the observation that AtSKs
331 such as BIN2 target TRAPPII, the question arises as to whether shaggy-like kinases regulate
332 differential growth decisions via TRS120 phosphorylation. To test this hypothesis, AtTRS120
333 phosphovariants homozygous for the null *trs120-4* allele and hemizygous for the phosphovariant
334 construct were studied under different environmental or stress conditions. The etiolation response
335 was not impacted by the phosphorylation status of AtTRS120 (Fig. S11). In contrast, TRS120
336 phosphomutants had phenotypes under additive stress conditions (Fig. 7D-F; Fig. S12). TRS120-
337 SαβγA non-phosphorylatable variants exhibited an enhanced root response under darkW
338 conditions (Fig. 7E) and a strongly enhanced ratio response to water stress in the dark (mean

339 RQ_{ratio} = 1.49; Fig. 7F). Conversely, the phosphomimetic TRS120-SαβγD mutants exhibited
340 severely attenuated responses to water stress in the dark in all respects (Fig. 7D-F; mean
341 $RQ_{hypocotyl}$= 0.66; mean RQ_{root} = 1.48; mean RQ_{ratio} = 0.44). Thus, the non-phosphorylatable
342 TRS120-SαβγA and the phosphomimetic TRS120-SαβγD mutations had opposite effects on
343 hypocotyl versus root lengths under water stress in the dark, with TRS120-SαβγA exhibiting an
344 enhanced and TRS120-SαβγD an attenuated ratio response (Fig. 7F). Under all environmental
345 conditions, the total seedling length of the phosphovariants did not significantly differ from that of
346 the wild-type AtTRS120 construct (Fig. S12D), which highlights the absence of a growth defect.
347 We conclude that the TRS120 phosphorylation status impacts the seedling's ability to differentially
348 regulate its hypocotyl and root lengths in response to additive stress conditions. Taken together,
349 the data show opposite impacts of non-phosphorylatable versus phosphomimetic mutations at
350 AtTRS120 AtSK sites in terms of (i) seed germination under osmotic stress and (ii) responses to
351 additive stress. This suggests that TRAPPII phosphorylation by shaggy-like kinases mediates
352 adaptive responses to osmotic stress and to light and water availability.
353
354
355 **DISCUSSION**
356 In this study, we explore the role of the TGN in stress responses in Arabidopsis. Our point of entry
357 is the TRAPPII complex, which has been shown to be required for TGN structure and function (Qi
358 *et al*, 2011; Ravikumar *et al*, 2018). We performed proteomic and yeast two-hybrid screens and
359 present several lines of *in vitro* (Y2H, kinase assays) and *in vivo* (IP-MS, pharmacological
360 inhibition) evidence that the TRAPPII subunit AtTRS120 is the target of AtSK kinases, including
361 BIN2. We document differential phosphorylation of three distinct AtSK/GSK3 sites by three of the
362 four AtSK clades. The phosphorylation status of AtTRS120 impacted seed germination under
363 osmotic stress as well as adaptive responses to additive stress. We show that *bin2* and *trappii*
364 alleles have related phenotypes with respect to an impaired adaptation to additive stress
365 conditions, in this instance achieved by the simultaneous withdrawal of light and water.
366 A concern when assessing the role of the TGN in stress responses is that TGN-related mutants
367 typically have pleiotropic phenotypes as a consequence of their impairment in fundamental
368 processes such as secretion, endocytosis or sorting (Rosquete & Drakakaki, 2018; Ravikumar *et*
369 *al*, 2018). To distinguish between primary defects in growth on the one hand and adaptive
370 responses on the other, we monitored trade-offs between hypocotyl and root growth under additive
371 stress conditions (Kalbfuß *et al*, 2022). We focus on *echidna* and *trappii* mutants as these have
372 been shown to impact both the structure and the function of the TGN (Boutté *et al*, 2013; Gendre

373 *et al*, 2011, 2013; McFarlane *et al*, 2013; Qi *et al*, 2011; Ravikumar *et al*, 2018). These TGN
374 mutants had hypocotyl and root growth defects, which are characteristic of trafficking mutants (Fig.
375 S8). In addition to their growth defects, *trappii trs120-4* mutants had a significant hypocotyl
376 response but in the wrong orientation as compared to the wild-type (denoted by red asterisks in
377 Fig. 4 and Fig. 5) as well as an insignificant hypocotyl/root ratio response to light and water
378 deprivation (Fig. 4). The *trappii* phenotypes described in this study are difficult to explain as mere
379 growth defects. Rather, the inability to mediate trade-offs in growth in response to additive stress
380 provides a compelling argument for TRAPPII as having a role in adaptive growth decisions.
381 Conceptually, the optimization of hypocotyl-to-root ratios can be deconstructed into four distinct
382 stages: (i) perception, (ii) signal integration, (iii) decision making and (iv) the implementation of
383 resulting actions (Kalbfuß *et al*, 2022). To address the first stage, perception, we looked at
384 quadruple *phyA phyB cry1 cry2* photoreceptor mutants; these failed to adjust their organ lengths
385 to light versus dark conditions but had a highly significant response to additive stress (Fig. 4G-H;
386 Fig. S8G-I; Kalbfuß *et al*, 2022). The opposite was true for *bin2-3 bil1 bil2* and *trappii* mutants,
387 which were able to respond to single stress factors but not to additive stress (Fig. 4; Kalbfuß *et al*,
388 2022). Shaggy-like kinases integrate a vast number of signaling pathways (Lv & Li, 2020; Youn &
389 Kim, 2015; Li *et al*, 2021; Song *et al*, 2023; Planas-Riverola *et al*, 2019). Accordingly, we have
390 postulated that the *bin2-3 bil1 bil2* „decision“ phenotype under conflict-of-interest scenarios is
391 primarily due to signal integration (Kalbfuß *et al*, 2022). Prime candidates for the fourth stage,
392 execution or implementation of the action, are *echidna* mutants; these had highly significant
393 adaptive responses - in the correct orientation - despite their growth defects (Fig. 4). The question
394 arises as to how to categorize *trappii* mutants in the above conceptual framework. Despite having
395 abnormally short hypocotyls or roots, *trappii* mutants still exhibited differential length increase
396 depending on light availability (Fig. S8). This shows that they are able to perceive and respond to
397 light.
398 If TRAPPII is primarily involved neither in perception nor in execution, this would place it at the
399 signal integration and/or decision-making steps of adaptive growth decisions. The TRAPPII
400 interactome is vast and complex, with - in addition to the expected ontologies describing traffic,
401 transport and cellular organization - a surprising number of signaling components implicated in
402 responses to abiotic cues (Fig. 1A). This suggests a role for TRAPPII in signal integration. A recent
403 study of the BIN2 signaling network describes the expected components of hormone signaling,
404 phototropism and stress responses; surprisingly, the BIN2 signaling network also includes
405 secretion, endocytosis, autophagy, TGN, endoplasmic reticulum (ER), cell wall and cytoskeleton
406 (Kim *et al*, 2023). Thus, there is a considerable compartmental overlap between the BIN2 network

407 and the TRAPPII interactome. Nonetheless, TRAPPII did not feature among the 482 members of
408 the BIN2 signaling network identified by proximity labeling (Kim *et al*, 2023). The discrepancy
409 could be due to the different methods used: yeast two hybrid and proteomics in this study versus
410 proximity labelling and phosphoproteomics in Kim *et al*, 2023. However, a multiomics approach
411 identified AtTRS120-S971 (encompassed by our identified β site AtTRS120-
412 S971:S973:S974:S975) as being differentially phosphorylated in response to brassinolide
413 treatment (Clark *et al*, 2021). This provides an additional line of *in vivo* evidence for a BIN2-
414 AtTRS120 interaction and suggests that TRAPPII phosphorylation is brassinosteroid-regulated, at
415 least for the AtTRS120-S971 residue.
416 BIN2 is a negative regulator of BR signaling and AtSK11 and AtSK12 have been shown to
417 negatively regulate root growth responses under osmotic stress (Dong *et al*, 2020; Li *et al*, 2021;
418 Song *et al*, 2023). To explore the biological significance of the AtSK-TRAPPII interaction, we
419 probed the phenotypes of TRAPPII phosphovariants. We found that these had an impact on
420 hypocotyl versus root growth tradeoffs in response to additive stress. Furthermore, the non-
421 phosphorylatable TRS120-SαβγA variant had an enhanced root adaptation whereas the
422 phosphomimetic variant decreased root growth under additive stress, which is consistent with the
423 negative regulation of growth by BIN2 and other AtSKs. We have previously described plant-
424 specific domains or subunits predicted to be at the dimer interface of the Arabidopsis TRAPPII
425 complex (marked in green in Fig. 2E; Garcia *et al*, 2020; Kalde *et al*, 2019). Interestingly, BIN2
426 interacts with the plant-specific C-terminal domain of AtTRS120, while MAP65-3 interacts with
427 plant-specific C-terminal domains of the TRAPPII-specific subunits CLUB and AtTRS120 (Steiner
428 *et al*, 2016). This presents intriguing implications regarding the potential role of the AtSK-TRAPPII
429 module in meeting the unique demands of endomembrane traffic in plants.
430 The observation that the *trappii* “decision” phenotype was not shared by *echidna* mutants raises
431 the question as to what facet of TGN function is required for responses to additive stress.
432 ECHIDNA and TRAPPII have been shown to have overlapping roles in basal TGN functions such
433 as secretion (Ravikumar *et al*, 2018). In addition, ECHIDNA regulates ER stress and immunity
434 whereas TRAPPII has roles in cytokinesis and in the establishment of cell polarity that appear to
435 be independent of ECHIDNA (Liu *et al*, 2023; Ravikumar *et al*, 2018). In the literature, there are
436 few examples of null mutants that are associated with the TGN and that have a positive influence
437 on growth. One such example is ZmBet5L1 (Zhao *et al*, 2023), which encodes a core subunit of
438 the TRAPPII complex (Kalde *et al*, 2019; Thellmann *et al*, 2010). Null alleles of ZmBet5L1 enhance
439 root growth also in the absence of stress (Zhao *et al*, 2023). The TRAPPII complex has two distinct
440 molecular functions: it acts as a tethering complex and as a Rab-GTPase guanine nucleotide

441 exchange factor (Rab-GEF). Rab-GEFs act as central cellular switches that turn GDP-bound
442 inactive Rab-GTPases to active GTP-bound forms (Elliott *et al*, 2020). Rab-GTPase cascades are
443 crucial for the development of polarity and directional growth in plants and play a vital role in
444 facilitating physiologically dynamic functions (Elliott *et al*, 2020). AtTRAPPII is thought to be a GEF
445 for the TGN-associated RabA-GTPases, a highly expanded class with 26 members (Kalde *et al*,
446 2019; Elliott *et al*, 2020). The TRAPPII interactome contains not only Rabs in the A class, but also
447 other classes of Rab GTPases such as RabF1, which is involved in stress responses (Yin *et al*,
448 2017). In contrast to ECHIDNA, which is required for the biogenesis of secretory vesicles and for
449 growth generically, as a putative Rab-A GEF TRAPPII has an ability to mediate all the highly
450 diverse facets of TGN function. In a judgement-decision model for plant behavior, judgment is a
451 composite of discrimination, assessment, recognition, and categorization (Karban & Orrock,
452 2018). In this context, it is interesting that the most expanded Rab GTPase family is TGN-
453 associated, suggestive of a tremendous degree of discrimination, specialization and
454 subcompartmentalization at the TGN.
455 Our study highlights the possible relevance of the AtSKs-TRAPPII interaction for adaptive growth
456 decisions (Fig. 8). Shaggy-like kinases such as BIN2 integrate a vast number of signaling
457 pathways and, together with receptor complexes at the cell surface, comprise a surveillance
458 system fine-tuned to both biotic and abiotic cues (Lv & Li, 2020; Planas-Riverola *et al*, 2019; Youn
459 & Kim, 2015; Li *et al*, 2021; Song *et al*, 2023). Via the cytosol, the AtSKs would then transmit this
460 information by mediating the phosphorylation status of the TRAPPII complex. TRAPPII would, in
461 turn, mediate TGN function. As an early endosome, the TGN is a central hub in the flow of
462 information to and from the cell surface. It is also intimately connected to the late endosome (or
463 the pre-vacuolar compartment) and to the Golgi, which provides complex polysaccharides as
464 building blocks for the deposition of new cell wall. Thus, the AtSK-TRAPPII interaction would
465 integrate all levels of cellular organization. We posit that signal integration and decision-making
466 occur at the AtSK-TRAPPII interface and that, downstream of TRAPPII, Rab GTPase cascades
467 are implicated in implementing decisions reached at the AtSK-TRAPPII module (Fig. 8). Sorting
468 and trafficking decisions at the TGN would enable plants to respond to developmental or
469 environmental signals via differential growth or various forms of movement.
470 Plants exhibit plasticity in their growth, meaning they can adjust their growth patterns in response
471 to environmental cues such as light, temperature, and nutrient availability. It has been argued that
472 plant phenotypic plasticity “is the result of signal integration - a process that requires cell-cell
473 communication, and that results in adaptive forms of movement not to be interpreted as automatic
474 and programmed” (Garzón & Keijzer, 2011). Movement in plants involving organ bending require

475 the polar distribution of morphogens such as auxin. This, in turn, requires the polarized localization
476 of auxin transporters such as PINs. The Arabidopsis TRAPPII complex has been shown to play a
477 pivotal role in a variety of sorting decisions including the polar localization of PIN2 proteins (Qi *et*
478 *al*, 2011; Rybak *et al*, 2014; Ravikumar *et al*, 2018). How environmental or developmental cues
479 regulate the cargo composition and sorting of TGN vesicles remains unclear. Future experiments
480 will explore the impact of the TRAPPII phosphorylation status on protein sorting, cell polarity, and
481 on the Rab specificity of TRAPPII as a putative GEF. The presence of the TOR kinase in the
482 TRAPPII interactome is intriguing, as TOR integrates information about nutrient and energy
483 availability, and has recently been shown to regulate actin dynamics as a function of ATP levels
484 (Dai *et al*, 2022); it is tempting to speculate that TOR could provide information on nutrient and
485 energy levels to the AtSK-TRAPPII "decision" module. In plants, the Trans-Golgi Network (TGN)
486 plays a critical role in the relay of information between the cell surface and intracellular
487 compartments. An AtSK-TRAPPII interaction would instruct the TGN, a central and highly
488 discriminate cellular hub, as to how to mobilize and allocate resources to optimize survival under
489 limiting or adverse conditions.
490

491 **EXPERIMENTAL PROCEDURES**
492
493 **Lines and growth conditions**
494 All the lines used in this study are listed in Table S1. Seedling-lethal mutants were propagated as
495 hetero- or hemi-zygotes. Insertion lines were selected via the TAIR and NASC web sites
496 (Swarbreck *et al*, 2008). Plants were grown in the greenhouse under controlled temperature
497 conditions and with supplemental light, or under controlled growth chamber conditions at the
498 TUMmesa ecotron (16/8 h photoperiod at 180 µmol $m^{-2}s^{-1}$). Seed were surface sterilized, stratified
499 at 4°C for two days and plated on ½ MS medium supplemented with 1% sucrose and B5 Vitamins
500 (Sigma; https://www.sigmaaldrich.com). Plates were incubated at 22°C in constant light (80 µmol
501 $m^{-2}s^{-1}$). The root tips of five-day-old plate-grown seedlings were used for confocal microscopy.
502 Seven-day-old plate-grown seedlings were used for co-immunoprecipitation.
503
504 **Co-immunoprecipitation (IP)**
505 For CLUB/AtTRS130:GFP we used 3 g of inflorescences per IP experiment. For TRS120-GFP, 3
506 g of light-grown seedlings were harvested at day 7. For bikinin treatment, seedlings were treated
507 for 30 min with 25 µM bikinin at day 7; mock treatments were conducted in parallel.
508 Co-immunoprecipitation experiments were carried out as described previously (Rybak *et al*, 2014).
509 Briefly, seedling lysates were incubated with GFP-trap beads (Chromotek). After washing away
510 all non-binding proteins, 70 µl 2x NuPAGE LDS + 25 mM dithiothreitol (DTT) buffer (ThermoFisher,
511 US) was added and boiled at 70°C for 10 min to denature the bait and all interaction partners.
512 In-gel trypsin digestion was performed according to standard procedures (Shevchenko *et al*,
513 2006). Briefly, the samples were run on a NuPAGE 4-12% Bis-Tris Protein Gel (Thermofisher
514 Scientific, US) for 3 min. Subsequently, the still not size-separated single protein band per sample
515 was cut out of the gel, reduced (50 mM DTT), alkylated (55 mM chloroacetamide) and digested
516 overnight with trypsin (trypsin-gold, Promega). The resulting peptides were analysed by mass
517 spectrometry. More detailed information on the mass-spectrometric data acquisition is provided in
518 the supporting method section.
519
520 **Molecular techniques and site directed mutagenesis (SDM)**
521 For subcloning for expression in *E.coli* or yeast, we used cDNA clones developed by the plant
522 genome project of RIKEN Genomic Sciences Center (Seki *et al*, 1998, 2002). Non-
523 phosphorylatable and phosphomimetic TRS120 phosphosite variant constructs (SαA, SβA, SγA,
524 SαβA, SαγA, SβγA, SαβγA and SαD, SβD, SγD, SαβD, SαβγD)) were generated using the
525 GATEWAY® cloning system and site-specific primers (see supplementary methods for substituted
526 amino acids and used primers). TRS120-T2 cDNA sequences (spanning amino acids 499-1187;
527 Rybak *et al*, 2014) were used as SDM template for protein expression in *Escherichia coli* (*E. coli*;
528 kinase assays) and in yeast (Y2H). For *in planta* experiments (confocal microscopy, IP-MS), the
529 genomic construct P_{TRS120}::TRS120-GFP (Rybak *et al*, 2014) was used as an SDM template.
530 TRS120 phosphovariants were introduced into plants via *Agrobacterium* mediated transformation
531 (see supplementary methods for further details).
532
533

534 **Yeast two-hybrid (Y2H)**
535 Y2H pairwise tests were performed as described in Altmann *et al*, 2018. Briefly, open reading
536 frames (ORFs) encoding CLUB/AtTRS130 truncations (C2, C3), TRS120 truncations (T1, T3) and
537 BIN2 were transferred by Gateway cloning into the GAL4 DNA-binding domain (DB) encoding
538 Y2H vector pDEST-pPC97, and subsequently transformed into the yeast strain Y8930. These
539 constructs were screened by yeast mating against a TRS120-T2 truncation and its
540 phosphomutants TRS120-T2- SαD, SβD, SγD, SαβD and SαβγD fused to the Gal4 activation
541 domain (AD) in the yeast strain Y8800. Interaction was assayed by growth on selective plates
542 using the *HIS3* reporter, and using 1 mM 3-Amino-1,2,4-triazole (3-AT) to suppress background
543 growth. All candidate interactions were verified by pairwise one-on-one mating in four independent
544 experiments. Only pairs scoring positives in all four assays were considered as *bona fide*
545 interaction partners.
546
547 ***In vitro* kinase assays**
548 Glutathione S-transferase (GST)-BIN2 (Li & Nam, 2002) and GST-T2-TRS120 phosphovariants
549 were expressed in *Escherichia coli* (Rosetta-gami™ strain) under constant shaking for 20 h at
550 25°C or 20 h at 18°C, respectively. The expressed proteins were affinity purified with GST-tags.
551 After sonication of the samples in 1x PBS, 1 mM PMSF, 1 mg/ml lysozyme and 1% Triton X-100,
552 the bacterial cell rests were centrifuged for 30 min at 16,000 g. Supernatants were incubated for
553 2 h with Glutathione Sepharose® 4 Fast Flow Beads (GE Healthcare) while rotating. After washing
554 the samples five times, the GST tagged proteins were eluted with 10 mM glutathione and
555 concentrated by ultra-filtration.
556 *In vitro* kinase assays with radiograph readout were performed as described previously (Kim *et al*,
557 2012), with some adaptations. In short, ca. 0.1 µg GST-BIN2 and ca. 0.5 µg of a GST-T2-TRS120
558 phosphovariant were incubated in 20 mM Tris pH 7.5, 1 mM $MgCl_2$, 100 mM NaCl, 1 mM DTT,
559 100 µM ATP and 10 µCi ATP[γ-^{32}P] for 3 h at 22°C in motion. The kinase reaction was stopped
560 by adding 2x SDS sample buffer and by boiling the samples for 10 min. Protein phosphorylation
561 was analyzed by autoradiographs and SDS-PAGE.
562 *In vitro* kinase assays with mass-spectrometry readout were performed to determine specific
563 phosphorylation sites. For each reaction, 10 µg of substrate (TRS120-T2) and different dilutions
564 of the kinase (1:5, 1:10, 1:100) were incubated for 15, 30, and 120 min in a kinase buffer (20 mM
565 Tris HCl, 100 mM NaCl, 1 mM $MgCl_2$, 1 mM DTT, 1 mM ATP). For the negative controls, one
566 sample with the highest kinase concentration and the longest incubation time was incubated in a
567 kinase buffer without ATP. For the kinase dead control, the kinase was heat-inactivated prior to
568 the incubation with its substrate. To stop the reaction, samples were heated at 95°C for 5 min.
569 After reduction (10 mM DTT), alkylation (55 mM CAA) and protein digestion (trypsin-gold,
570 Promega) the resulting peptides were purified using self-packed StageTips (C18 material, 3M
571 Empore) and analyzed by mass spectrometry. More detailed information can be found in the
572 supporting methods.
573
574 **LC-MS/MS data acquisition and analysis**
575 Generated peptides were analyzed on a Dionex Ultimate 3000 RSLCnano system coupled to a
576 Q-Exactive HF-X mass spectrometer (Thermo Fisher Scientific) in data-dependent acquisition
577 mode. Peptide identification and quantification was performed using the software MaxQuant

578 (version 1.6.1.0) (Cox & Mann, 2008; Tyanova *et al*, 2016a) with its built-in search engine
579 Andromeda (Cox *et al*, 2011) and an *Arabidopsis thaliana* reference database (Araport). Perseus
580 (Tyanova *et al*, 2016b) and Python 3.0 were used for statistical data analyses. For a targeted
581 analysis of the kinase assay data set, MS1 chromatograms from selected phosphopeptides were
582 extracted and analyzed using the Skyline software (MacLean *et al*, 2010). For detailed information
583 about LC-MS/MS data acquisition and analysis see supporting methods.
584
585 **Light and electron microscopy**
586 For scanning electron microscopy, a Zeiss (LEO) VP 438 microscope was operated at 15 kV.
587 Fresh seedlings were placed onto stubs and examined immediately in low vacuum. Confocal
588 microscopes used for imaging were an Olympus (www.olympus-ims.com) Fluoview 1000 confocal
589 laser scanning microscope (CSLM) and a Leica (www.leica-microsystems.com) SP8 Hyvolution
590 CSLM. 40x and 60x water immersion 0.9 numerical aperture objectives (Olympus) were used.
591 Imaging data were acquired using LAS-X software (Leica) and FV10-Ver.2.6.0 software
592 (Olympus). The following excitation and emission parameters were used for the respective
593 fluorescent proteins: YFP 514 nm excitation, 525-575 nm emission; GFP 488 nm excitation, 500-
594 550 nm emission; and FM4-64 emission at 640 nm. 10-day-old seedlings were stained with
595 modified pseudo-Schiff propidium iodide staining (Truernit *et al*, 2008). Excitation Laser was set
596 to 488 nm. The Emission was detected at 520 nm. The junction between the meristematic and
597 elongation zones was determined by marking the first cell in a single cortex cell file that was double
598 the length of the previous cell (González-García *et al*, 2011). For seedling images, a Leica S APO
599 stereo microscope with a Leica MC170 HD camera was used.
600
601 **Differential growth decision assay**
602 The differential growth decision experiment was performed as described by Kalbfuß *et al*, 2022.
603 In brief, seeds were surface sterilized using a brief 80% ethanol rinse followed by 15 min
604 incubation in sterilization buffer (0.01% SDS, 3% NaOCl). After 5 washes in mQ water, seeds
605 were resuspended in 0.15% agar and stratified in the dark at 4°C for 7 days to break seed
606 dormancy. Afterwards, seeds were plated on squared plates with exactly 45 ml ½ MS medium
607 supplemented with B5 Vitamins (Sigma). Culture media for TRS120 phosphomutants was
608 additionally supplemented with 50 µg/ml kanamycin to select for transgenic seedlings. For -0.4
609 MPa water deficit, media plates were infused with sterile-filtrated 45 ml 2x PEG-6000 (Merck
610 group; dissolved in liquid ½ MS media) for exactly 24 h at RT and afterwards the PEG-solution
611 completely decanted. Seeds were plated at the interface between the culture media and sterilized
612 plastic strips on the media such that, upon germination, only the root touched the agar. For water
613 stress, seeds in each biological replicate were sown on two plates for technical replicates which
614 were pooled for analysis. After plating plates were sealed with breathable tape. Plates for dark
615 conditions were wrapped with two layers of thick aluminum foil. All plates were incubated for 10
616 days at 22°C with permanent light (80 µmol $m^{-2}s^{-1}$). Note that the plates were negatively inclined
617 by 4° to promote root growth on the media surface rather than in the agar.
618 After incubation of 10 days seedlings were transferred onto cold 1.2% agar plates, scanned at
619 1200 ppi and saved as tiff files. Hypocotyl and root lengths were analyzed with Fiji - ImageJ using
620 the free-hand-tool. The ratio was calculated as hypocotyl length divided by root length.

621 Root and hypocotyl responses to water deficit in the dark (abbreviated as darkW) were
622 computed as

623 $$\frac{\text{organ length in the dark}}{\text{organ length under darkW}}$$

624

625 And for the ratio:

626 $$\text{ratio adjustment}=\frac{\left(\frac{\text{hypocotyl}}{\text{root}}\right)\text{dark}}{\left(\frac{\text{hypocotyl}}{\text{root}}\right)\text{darkW}}$$

627 Due to variability between PEG lots and PEG plates (Kalbfuß *et al*, 2022), we normalized each
628 mutant to the corresponding wild-type ecotype (see Table S1) on the same plate. Thus, the
629 normalized ratio adjustment to water stress in the dark (darkW) was computed as follows:

630 $$RQ_{ratio}=\frac{\text{ratio adjustment mutant}}{\text{ratio adjustment wild-type}}$$

631

632 $RQ_{hypocotyl}$ and RQ_{root} as well as light versus dark responses were computed in a similar fashion.
633 These normalized organ and ratio adjustments were referred to as response quotients (RQ) to
634 light-to-dark or dark-to-darkW conditions. The mean RQ_{ratio} of at least three biological replicates
635 (i.e. the seed stocks from different mother plants) is shown. Responses were considered to be
636 attenuated for $RQ_{ratio} < 0.8$, normal in the 0.8-1.2 range, and enhanced for $RQ_{ratio} > 1.2$. For volcano
637 plots we plotted the mean RQ_{ratio} on the X axis and the median P_{ratio}-value on the Y axis. Organ
638 and ratio adjustments for light-to-dark comparisons were computed as organ length (or ratio) in
639 the light divided by organ length (or ratio) in the dark. P-values were computed with the Student's
640 T-test. Responses were considered to be insignificant for P-values ≥ 0.05 and attenuated for P-
641 values ≥ 0.00001. The median P-value for at least three replicates is shown in the volcano plots.

642

643 **Germination assay under osmotic stress**

644 For germination curve experiments, surface-sterilized seeds were stratified in the dark at 4°C for
645 two days. Seeds were plated on ½ MS media supplemented with 0.05% B5 Vitamins (Sigma) and
646 either 0 mM, 200 mM, or 400 mM mannitol (Millipore). Approximately 100 seeds were plated per
647 condition. Plates were incubated at 22°C under constant light conditions (80 µmol $m^{-2}s^{-1}$) and
648 rotated every day. Seed germination rates were recorded every 24 h. Seeds were scored as
649 germinated when the radicle emerged. Data were obtained for three biological replicates, each
650 with three technical replicates.

651

652 **Western blot analysis**

653 Standard Western blot analysis was performed according to Sambrook *et al*, (1989). 7.5% SDS-
654 PAGE gels (Mini-PROTEAN TGX gels, Bio-Rad) were blotted onto PVDF Immobilon-FL
655 membranes (Millipore). Polyclonal rabbit anti-GFP antibody (1:2000; A11122, Invitrogen) was
656 used as primary antibody. As secondary antibody, we used a goat anti-rabbit Horseradish
657 peroxidase-conjugated antibody (1:6000; Pierce, Thermo Scientific) together with the SuperSignal
658 West Femto Maximum Sensitivity Substrate (Thermo Scientific). To check for equal loading, blots
659 were stained with Coomassie (10% acetic acid, 50% methanol, 0.25% Coomassie Blue R-250)
660 and subsequently destained (10% acetic acid, 50% methanol).

Statistical analysis and image processing

False discovery rates, determined with the standard two-tailed t-test, were set at a cut-off of 1. Images taken with the Leica SP8 microscope were deconvolved using the built-in Huygens Scientific deconvolution software (www.leica-microsystems.com) operated in 2D. For consistency in quantitative analyses, we selected cortical root tip cells, at a height of 6-22 cells above the quiescent center in the root apical meristem. Images were processed with Adobe photoshop (www.adobe.com) and GIMP (https://www.gimp.org) and analysed with Image J (https://imagej.nih.gov). Statistical analyses were performed in RStudio. Figures were created with RStudio's ggplot2 package and assembled with Inkscape (https://inkscape.org).

Acknowledgements

We thank Prof. Wilfried Schwab, Prof. Erwin Grill and other members of the botany department for their support. Thanks to Prof. Arne Skerra, Martin Schlapschy and Veder Garcia for useful suggestions. We thank Yannik Schreckenberg, Andreas Czempiel, Hermine Kienberger, Nina Lomp and Franziska Hackbarth for technical assistance. We thank the WZW/TUM Centre for Advanced Light Microscopy (CALM), headed by Ramon Torres-Ruiz and Klaus Michel, for access to confocal microscopes, and Prof. Kay Schneitz for access to their Leica S APO stereo microscope. Thanks to Roman Meier at the TUMmesa facility, directed by Leonardo Teixeira, for supporting us with optimal growth conditions for our plants. Jorge José Casal and Sean Cutler shared published resources.

Data deposition

Mass spectrometry data have been deposited with the ProteomeXchange Consortium via the PRoteomics IDEntification (PRIDE) partner repository (Perez-Riverol *et al*, 2019) or the Mass Spectrometry Interactive Virtual Environment data repository (MassIVE; http://massive.ucsd.edu). The CLUB-GFP IP-MS data can be accessed with the dataset identifier PXD013016. The proteomics raw data, MaxQuant search results and used protein sequence databases for the other datasets can be accessed using the MassIVE data set identifier [pending]. All targeted proteomic raw data and Skyline analysis files have been deposited to Panorama Public (Sharma *et al*, 2014, 2018) [pending].

Funding

This work was supported by Deutsche Forschungsgemeinschaft DFG grants AS110/5-2, AS110/8-1 & AS110/10-1 as well as BaCaTEC Nr. 14 [2018-2] to F.F.A., and by the European Research Council's Horizon 2020 Research and Innovation Programme (Grant Agreement 648420) grant to P.F-B. M. Abele and C.L. were supported by the EU Horizon 2020 grant Epic-XS. TUMmesa was funded with support of the German Science Foundation (DFG, INST 95/1184-1 FUGG).

Conflict of interest

The authors declare no conflict of interest.

Author contributions

Conceptualization: FFA
Methodology: MA, CL, BA, CHP, PFB, CW, AS, NK, ASM, BB, CM, EF, FFA
Investigation: CW, MA, BA, MAM, AS, NK, ASM, RR, CHP, BB, CM, EF, FFA
Visualization: CW, MA, BA, MAM, AS, NK, ASM, RR, CHP, BB, CM
Funding acquisition: DWE, PFB, ZW, CL, FFA
Project administration: FFA
Supervision: EF, DWE, PFB, ZW, CL, FFA
Writing - original draft: FFA
Writing - review & editing: CW, MA, BA, NK, ASM, RR, CHP, BB, CM, PFB, ZW, CL, FFA

720 **REFERENCES**

721

722 Altmann M, Altmann S, Falter C & Falter-Braun P (2018) High-Quality Yeast-2-Hybrid Interaction
723 Network Mapping. *Curr Protoc Plant Biol* 3: e20067
724 Asaoka R, Uemura T, Ito J, Fujimoto M, Ito E, Ueda T & Nakano A (2013) Arabidopsis RABA1
725 GTPases are involved in transport between the trans-Golgi network and the plasma
726 membrane, and are required for salinity stress tolerance. *Plant J* 73: 240–249
727 Assaad FF, Huet Y, Mayer U & Jürgens G (2001) The Cytokinesis Gene KEULE Encodes a Sec1
728 Protein That Binds the Syntaxin KNOLLE. *J Cell Biol* 152: 531–543
729 Boutté Y, Jonsson K, McFarlane HE, Johnson E, Gendre D, Swarup R, Friml J, Samuels L, Robert
730 S & Bhalerao RP (2013) ECHIDNA-mediated post-Golgi trafficking of auxin carriers for
731 differential cell elongation. *Proc Natl Acad Sci U S A* 110: 16259–16264
732 Cai Y, Chin HF, Lazarova D, Menon S, Fu C, Cai H, Sclafani A, Rodgers DW, De La Cruz EM,
733 Ferro-Novick S, *et al* (2008) The Structural Basis for Activation of the Rab Ypt1p by the
734 TRAPP Membrane-Tethering Complexes. *Cell* 133: 1202–1213
735 Clark NM, Nolan TM, Wang P, Song G, Montes C, Valentine CT, Guo H, Sozzani R, Yin Y &
736 Walley JW (2021) Integrated omics networks reveal the temporal signaling events of
737 brassinosteroid response in Arabidopsis. *Nat Commun* 12: 5858
738 Cox J & Mann M (2008) MaxQuant enables high peptide identification rates, individualized p.p.b.-
739 range mass accuracies and proteome-wide protein quantification. *Nat Biotechnol* 26: 1367–
740 1372
741 Cox J, Neuhauser N, Michalski A, Scheltema RA, Olsen J V. & Mann M (2011) Andromeda: A
742 Peptide Search Engine Integrated into the MaxQuant Environment. *J Proteome Res* 10:
743 1794–1805
744 Dai L, Wang B, Wang T, Meyer EH, Kettel V, Hoffmann N, McFarlane HE, Li S, Wu X, Picard KL,
745 *et al* (2022) The TOR complex controls ATP levels to regulate actin cytoskeleton dynamics
746 in Arabidopsis. *Proc Natl Acad Sci U S A* 119: e2122969119
747 Darwin C (2009) The Power of Movement in Plants Cambridge University Press
748 Ding Z, Galván-Ampudia CS, Demarsy E, Łangowski Ł, Kleine-Vehn J, Fan Y, Morita MT, Tasaka
749 M, Fankhauser C, Offringa R, *et al* (2011) Light-mediated polarization of the PIN3 auxin
750 transporter for the phototropic response in Arabidopsis. *Nat Cell Biol* 13: 447–452
751 Dong L, Wang Z, Liu J & Wang X (2020) AtSK11 and AtSK12 Mediate the Mild Osmotic Stress-
752 Induced Root Growth Response in Arabidopsis. *Int J Mol Sci* 21: 1–16
753 Elliott L, Moore I & Kirchhelle C (2020) Spatio-temporal control of post-Golgi exocytic trafficking in
754 plants. *J Cell Sci* 133: jcs237065
755 Ericsson T (1995) Growth and shoot: root ratio of seedlings in relation to nutrient availability. *Plant*
756 *Soil* 168: 205–214
757 Fan X, Yang C, Klisch D, Ferguson A, Bhaellero RP, Niu X & Wilson ZA (2014) ECHIDNA Protein
758 Impacts on Male Fertility in Arabidopsis by Mediating trans-Golgi Network Secretory
759 Trafficking during Anther and Pollen Development. *Plant Physiol* 164: 1338–1349
760 Friml J, Wiśniewska J, Benková E, Mendgen K & Palme K (2002) Lateral relocation of auxin efflux
761 regulator PIN3 mediates tropism in Arabidopsis. *Nature* 415: 806–809
762 Galviz YCF, Ribeiro R V. & Souza GM (2020) Yes, plants do have memory. *Theor Exp Plant*
763 *Physiol* 32: 195–202
764 Garcia VJ, Xu S-L, Ravikumar R, Wang W, Elliott L, Gonzalez E, Fesenko M, Altmann M,
765 Brunschweiger B, Falter-Braun P, *et al* (2020) TRIPP Is a Plant-Specific Component of the
766 Arabidopsis TRAPPII Membrane Trafficking Complex with Important Roles in Plant
767 Development. *Plant Cell* 32: 2424–2443
768 Garzón PC & Keijzer F (2011) Plants: Adaptive behavior, root-brains, and minimal cognition. *Adapt*
769 *Behav* 19: 155–171
770 Gendre D, Jonsson K, Boutté Y & Bhalerao RP (2015) Journey to the cell surface—the central

771 role of the trans-Golgi network in plants. *Protoplasma* 252: 385–398
772 Gendre D, McFarlane HE, Johnson E, Mouille G, Sjödin A, Oh J, Levesque-Tremblay G,
773 Watanabe Y, Samuels L & Bhalerao RP (2013) Trans-Golgi Network Localized
774 ECHIDNA/Ypt Interacting Protein Complex Is Required for the Secretion of Cell Wall
775 Polysaccharides in Arabidopsis. *Plant Cell* 25: 2633–2646
776 Gendre D, Oh J, Boutté Y, Best JG, Samuels L, Nilsson R, Uemura T, Marchant A, Bennett MJ,
777 Grebe M, *et al* (2011) Conserved Arabidopsis ECHIDNA protein mediates trans-Golgi-
778 network trafficking and cell elongation. *Proc Natl Acad Sci U S A* 108: 8048–8053
779 González-García M-P, Vilarrasa-Blasi J, Zhiponova M, Divol F, Mora-García S, Russinova E &
780 Caño-Delgado AI (2011) Brassinosteroids control meristem size by promoting cell cycle
781 progression in Arabidopsis roots. *Development* 138: 849–859
782 Jaber E, Thiele K, Kindzierski V, Loderer C, Rybak K, Jürgens G, Mayer U, Söllner R, Wanner G
783 & Assaad FF (2010) A putative TRAPPII tethering factor is required for cell plate assembly
784 during cytokinesis in Arabidopsis. *New Phytol* 187: 751–763
785 Jiménez JL, Hegemann B, Hutchins JRA, Peters J-M & Durbin R (2007) A systematic comparative
786 and structural analysis of protein phosphorylation sites based on the mtcPTM database.
787 *Genome Biol* 8: R90
788 Jumper J, Evans R, Pritzel A, Green T, Figurnov M, Ronneberger O, Tunyasuvunakool K, Bates
789 R, Žídek A, Potapenko A, *et al* (2021) Highly accurate protein structure prediction with
790 AlphaFold. *Nature* 596: 583–589
791 Kalbfuß N, Strohmayr A, Kegel M, Le L, Grosse-Holz F, Brunschweiger B, Stöckl K, Wiese C,
792 Franke C, Schiestl C, *et al* (2022) A role for brassinosteroid signalling in decision-making
793 processes in the Arabidopsis seedling. *PLoS Genet* 18: e1010541
794 Kalde M, Elliott L, Ravikumar R, Rybak K, Altmann M, Klaeger S, Wiese C, Abele M, Al B, Kalbfuß
795 N, *et al* (2019) Interactions between Transport Protein Particle (TRAPP) complexes and Rab
796 GTPases in Arabidopsis. *Plant J* 100: 279–297
797 Karban R & Orrock JL (2018) A judgment and decision-making model for plant behavior. *Ecology*
798 99: 1909–1919
799 Kim S-J & Bassham DC (2011) TNO1 Is Involved in Salt Tolerance and Vacuolar Trafficking in
800 Arabidopsis. *Plant Physiol* 156: 514–526
801 Kim T-W, Michniewicz M, Bergmann DC & Wang Z-Y (2012) Brassinosteroid regulates stomatal
802 development by GSK3-mediated inhibition of a MAPK pathway. *Nature* 482: 419–422
803 Kim T-W, Park CH, Hsu C-C, Kim Y-W, Ko Y-W, Zhang Z, Zhu J-Y, Hsiao Y-C, Branon T, Kaasik
804 K, *et al* (2023) Mapping the signaling network of BIN2 kinase using TurboID-mediated biotin
805 labeling and phosphoproteomics. *Plant Cell* 35: 975–993
806 Lee C-F, Pu H-Y, Wang L-C, Sayler RJ, Yeh C-H & Wu S-J (2006) Mutation in a homolog of yeast
807 Vps53p accounts for the heat and osmotic hypersensitive phenotypes in Arabidopsis hit1-1
808 mutant. *Planta* 224: 330–338
809 Li C, Zhang B & Yu H (2021) GSK3s: nodes of multilayer regulation of plant development and
810 stress responses. *Trends Plant Sci* 26: 1286–1300
811 Li J & Nam KH (2002) Regulation of Brassinosteroid Signaling by a GSK3/SHAGGY-Like Kinase.
812 *Science* 295: 1299–1301
813 Liu L, Qin L, Safdar L Bin, Zhao C, Cheng X, Xie M, Zhang Y, Gao F, Bai Z, Huang J, *et al* (2023)
814 The plant trans-Golgi network component ECHIDNA regulates defense, cell death, and
815 endoplasmic reticulum stress. *Plant Physiol* 191: 558–574
816 Lv M & Li J (2020) Molecular Mechanisms of Brassinosteroid-Mediated Responses to Changing
817 Environments in Arabidopsis. *Int J Mol Sci* 21: 2737
818 MacLean B, Tomazela DM, Shulman N, Chambers M, Finney GL, Frewen B, Kern R, Tabb DL,
819 Liebler DC & MacCoss MJ (2010) Skyline: an open source document editor for creating and
820 analyzing targeted proteomics experiments. *Bioinformatics* 26: 966–968
821 McClung CR (2006) Plant Circadian Rhythms. *Plant Cell* 18: 792–803

822 McFarlane HE, Watanabe Y, Gendre D, Carruthers K, Levesque-Tremblay G, Haughn GW,
823 Bhalerao RP & Samuels L (2013) Cell Wall Polysaccharides are Mislocalized to the Vacuole
824 in echidna Mutants. *Plant Cell Physiol* 54: 1867–1880
825 Naramoto S, Nodzyński T, Dainobu T, Takatsuka H, Okada T, Friml J & Fukuda H (2014) VAN4
826 Encodes a Putative TRS120 That is Required for Normal Cell Growth and Vein Development
827 in Arabidopsis. *Plant Cell Physiol* 55: 750–763
828 Perez-Riverol Y, Csordas A, Bai J, Bernal-Llinares M, Hewapathirana S, Kundu DJ, Inuganti A,
829 Griss J, Mayer G, Eisenacher M, *et al* (2019) The PRIDE database and related tools and
830 resources in 2019: improving support for quantification data. *Nucleic Acids Res* 47: D442–
831 D450
832 Pinar M, Arias-Palomo E, de los Ríos V, Arst HNJ & Peñalva MA (2019) Characterization of
833 Aspergillus nidulans TRAPPs uncovers unprecedented similarities between fungi and
834 metazoans and reveals the modular assembly of TRAPPII. *PLoS Genet* 15: e1008557
835 Planas-Riverola A, Gupta A, Betegón-Putze I, Bosch N, Ibañes M & Caño-Delgado AI (2019)
836 Brassinosteroid signaling in plant development and adaptation to stress. *Development* 146:
837 dev151894
838 Polko JK, van Zanten M, van Rooij JA, Marée AFM, Voesenek LACJ, Peeters AJM & Pierik R
839 (2012) Ethylene-induced differential petiole growth in Arabidopsis thaliana involves local
840 microtubule reorientation and cell expansion. *New Phytol* 193: 339–348
841 Qi X, Kaneda M, Chen J, Geitmann A & Zheng H (2011) A specific role for Arabidopsis TRAPPII
842 in post-Golgi trafficking that is crucial for cytokinesis and cell polarity. *Plant J* 68: 234–248
843 Rauf M, Arif M, Fisahn J, Xue G-P, Balazadeh S & Mueller-Roeber B (2013) NAC Transcription
844 Factor SPEEDY HYPONASTIC GROWTH Regulates Flooding-Induced Leaf Movement in
845 Arabidopsis. *Plant Cell* 25: 4941–4955
846 Ravikumar R, Kalbfuß N, Gendre D, Steiner A, Altmann M, Altmann S, Rybak K, Edelmann H,
847 Stephan F, Lampe M, *et al* (2018) Independent yet overlapping pathways ensure the
848 robustness and responsiveness of trans-Golgi network functions in Arabidopsis.
849 *Development* 145: dev169201
850 Ravikumar R, Steiner A & Assaad FF (2017) Multisubunit tethering complexes in higher plants.
851 *Curr Opin Plant Biol* 40: 97–105
852 Rosquete MR & Drakakaki G (2018) Plant TGN in the stress response: a compartmentalized
853 overview. *Curr Opin Plant Biol* 46: 122–129
854 Rosquete MR, Worden N, Ren G, Sinclair RM, Pfleger S, Salemi M, Phinney BS, Domozych D,
855 Wilkop T & Drakakaki G (2019) AtTRAPPC11/ROG2: A Role for TRAPPs in Maintenance of
856 the Plant Trans-Golgi Network/Early Endosome Organization and Function. *Plant Cell* 31:
857 1879–1898
858 Rybak K, Steiner A, Synek L, Klaeger S, Kulich I, Facher E, Wanner G, Kuster B, Zarsky V,
859 Persson S, *et al* (2014) Plant Cytokinesis Is Orchestrated by the Sequential Action of the
860 TRAPPII and Exocyst Tethering Complexes. *Dev Cell* 29: 607–620
861 Sambrook J, Fritsch EF & Maniatis T (1989) Molecular Cloning: A Laboratory Manual Cold Spring
862 Harbor Laboratory Press
863 Seki M, Carninci P, Nishiyama Y, Hayashizaki Y & Shinozaki K (1998) High-efficiency cloning of
864 Arabidopsis full-length cDNA by biotinylated CAP trapper. *Plant J* 15: 707–720
865 Seki M, Narusaka M, Kamiya A, Ishida J, Satou M, Sakurai T, Nakajima M, Enju A, Akiyama K,
866 Oono Y, *et al* (2002) Functional Annotation of a Full-Length Arabidopsis cDNA Collection.
867 *Science* 296: 141–145
868 Severino LS (2021) Plants make smart decisions in complex environments. *Plant Signal Behav*
869 16: 1970448
870 Sharma V, Eckels J, Schilling B, Ludwig C, Jaffe JD, MacCoss MJ & MacLean B (2018) Panorama
871 Public: A Public Repository for Quantitative Data Sets Processed in Skyline. *Mol Cell*
872 *Proteomics* 17: 1239–1244

873 Sharma V, Eckels J, Taylor GK, Shulman NJ, Stergachis AB, Joyner SA, Yan P, Whiteaker JR,
874 Halusa GN, Schilling B, *et al* (2014) Panorama: A Targeted Proteomics Knowledge Base. *J*
875 *Proteome Res* 13: 4205–4210
876 Shevchenko A, Tomas H, Havli J, Olsen J V & Mann M (2006) In-gel digestion for mass
877 spectrometric characterization of proteins and proteomes. *Nat Protoc* 1: 2856–2860
878 Silvertown J & Gordon DM (1989) A Framework for Plant Behavior. *Annu Rev Ecol Syst* 20: 349–
879 366
880 Söllner R, Glässer G, Wanner G, Somerville CR, Jürgens G & Assaad FF (2002) Cytokinesis-
881 Defective Mutants of Arabidopsis. *Plant Physiol* 129: 678–690
882 Song Y, Wang Y, Yu Q, Sun Y, Zhang J, Zhan J & Ren M (2023) Regulatory network of GSK3-
883 like kinases and their role in plant stress response. *Front Plant Sci* 14: 1123436
884 Steiner A, Rybak K, Altmann M, McFarlane HE, Klaeger S, Nguyen N, Facher E, Ivakov A, Wanner
885 G, Kuster B, *et al* (2016) Cell cycle-regulated PLEIADE/AtMAP65-3 links membrane and
886 microtubule dynamics during plant cytokinesis. *Plant J* 88: 531–541
887 Swarbreck D, Wilks C, Lamesch P, Berardini TZ, Garcia-Hernandez M, Foerster H, Li D, Meyer
888 T, Muller R, Ploetz L, *et al* (2008) The Arabidopsis Information Resource (TAIR): gene
889 structure and function annotation. *Nucleic Acids Res* 36: D1009–D1014
890 Thellmann M, Rybak K, Thiele K, Wanner G & Assaad FF (2010) Tethering Factors Required for
891 Cytokinesis in Arabidopsis. *Plant Physiol* 154: 720–732
892 Thomas LL, van der Vegt SA & Fromme JC (2019) A Steric Gating Mechanism Dictates the
893 Substrate Specificity of a Rab-GEF. *Dev Cell* 48: 100–114
894 Truernit E, Bauby H, Dubreucq B, Grandjean O, Runions J, Barthélémy J & Palauqui J-C (2008)
895 High-Resolution Whole-Mount Imaging of Three-Dimensional Tissue Organization and Gene
896 Expression Enables the Study of Phloem Development and Structure in Arabidopsis. *Plant*
897 *Cell* 20: 1494–1503
898 Tyanova S, Temu T & Cox J (2016a) The MaxQuant computational platform for mass
899 spectrometry-based shotgun proteomics. *Nat Protoc* 11: 2301–2319
900 Tyanova S, Temu T, Sinitcyn P, Carlson A, Hein MY, Geiger T, Mann M & Cox J (2016b) The
901 Perseus computational platform for comprehensive analysis of (prote)omics data. *Nat*
902 *Methods* 13: 731–740
903 Uemura T (2016) Physiological Roles of Plant Post-Golgi Transport Pathways in Membrane
904 Trafficking. *Plant Cell Physiol* 57: 2013–2019
905 Uemura T, Ueda T & Nakano A (2012) The physiological role of SYP4 in the salinity and osmotic
906 stress tolerances. *Plant Signal Behav* 7: 1118–1120
907 Varadi M, Anyango S, Deshpande M, Nair S, Natassia C, Yordanova G, Yuan D, Stroe O, Wood
908 G, Laydon A, *et al* (2022) AlphaFold Protein Structure Database: massively expanding the
909 structural coverage of protein-sequence space with high-accuracy models. *Nucleic Acids Res*
910 50: D439–D444
911 Wang L-C, Tsai M-C, Chang K-Y, Fan Y-S, Yeh C-H & Wu S-J (2011) Involvement of the
912 Arabidopsis HIT1/AtVPS53 tethering protein homologue in the acclimation of the plasma
913 membrane to heat stress. *J Exp Bot* 62: 3609–3620
914 Whippo CW & Hangarter RP (2009) The 'sensational' power of movement in plants: A Darwinian
915 system for studying the evolution of behavior. *Am J Bot* 96: 2115–2127
916 Yin C, Karim S, Zhang H & Aronsson H (2017) Arabidopsis RabF1 (ARA6) Is Involved in Salt
917 Stress and Dark-Induced Senescence (DIS). *Int J Mol Sci* 18: 309
918 Youn J-H & Kim T-W (2015) Functional Insights of Plant GSK3-like Kinases: Multi-Taskers in
919 Diverse Cellular Signal Transduction Pathways. *Mol Plant* 8: 552–565
920 Zhao R, Li N, Lin Q, Li M, Shen X, Peng Y, Du Y, Ning Q, Li Y, Zhan J, *et al* (2023) ZmBET5L1
921 inhibits primary root growth and decreases osmotic stress tolerance by mediating vesicle
922 aggregation and tethering in maize. *Plant Cell Environ* 46: 975–990
923 Zhu J, Gong Z, Zhang C, Song C-P, Damsz B, Inan G, Koiwa H, Zhu J-K, Hasegawa PM &

924 Bressan RA (2002) OSM1/SYP61: A Syntaxin Protein in Arabidopsis Controls Abscisic Acid-
925 Mediated and Non-Abscisic Acid-Mediated Responses to Abiotic Stress. *Plant Cell* 14: 3009–
926 3028
927

928 **FIGURE LEGENDS**

929

930 **Figure 1. The TRAPPII interactome.**

931 **A.** Gene ontology (GO) term enrichment analysis of the TRAPPII interactome. Depicted are fold
932 enrichments of GO terms of level 0 as bar plots colored by significance level. The data are derived
933 from an analysis of IP-MS from inflorescences with the TRAPPII-specific subunit CLUB-GFP as
934 bait (see Fig. 1B; Kalde *et al*, 2019). Terms are grouped by manually annotated super-categories.
935 Metabolic processes were excluded for simplification. Note that the super categories organization
936 (9) and traffic/transport (12) make up the majority of GO terms (21/49) and that response to
937 stimulus (11) comprises the second largest category. Cutoffs were set at 1.5 for fold-change and
938 0.003 for the *P*-value, which was adjusted for the false discovery rate.

939 **B.** IP-MS with the TRAPPII-specific subunit CLUB-GFP as bait (Kalde *et al*, 2019). Inflorescences
940 were used. Each protein was present in all three biological replicates. The ratio (or fold-change)
941 was calculated for each protein as the average intensity of the signal in the experiment divided by
942 its average intensity in the soluble GFP empty vector control. The *P*-value (depicted along a
943 negative log10 scale) is plotted against the signal ratio. Dotted grey lines represent cutoffs: *P*-
944 value < 0.02 and Ratio > 8 or > 5. Note that TRAPPII subunits (light blue for core TRAPP; dark
945 blue for TRAPPII-specific subunits; the AtTRS130/CLUB-GFP TRAPPII-specific bait is depicted
946 as an open circle) are in the upper right field, indicating high abundance and good reproducibility.
947 AtSKs (magenta), MAP65-1 (orange) and Rab A2a GTPase (green) are all in the upper middle
948 field; these may be transient interactors of TRAPPII. Note that AtSKs (AtSK11/12/32) are more
949 significant than validated interactors such as MAP65 and RabA2a (Kalde *et al*, 2019; Steiner *et*
950 *al*, 2016).

951 **C.** Yeast two-hybrid assays of interactions between BIN2 and TRAPPII subunits. BIN2 was fused
952 to the GAL4 DNA-binding domain (DB) and TRAPPII subunits and truncations thereof ($CLUB^{1-417}$,
953 $CLUB^{392-1260}$, $CLUB^{792-1260}$, $TRS120^{1-800}$, $TRS120^{499-1187}$ and $TRS120^{750-1187}$; referred to below as
954 CLUB-C1, -C2, -C3 and TRS120-T1, -T2, -T3) to the GAL4 activation domain (AD). As negative
955 control, the BIN2-DB construct was tested with the empty AD vector. Interactions were verified by
956 pairwise one-on-one mating in four independent replicate experiments. The panels are from
957 different plates. The results show interactions between BIN2 and $AtTRS120^{499-1187}$ wild-type. BIN2
958 bound specifically to the TRAPPII subunit TRS120 ($TRS120^{499-1187}$ / T2 truncation) and not with
959 other TRAPPII subunits or truncations. In a total of > 2400 pairwise tests, BIN2 was the only kinase
960 we found that interacted with a TRAPP subunit. The Y2H did not detect AtTRS130/CLUB-BIN2
961 interaction shown in Fig. 1B, which shows co-purified proteins that can include indirect - as

962 opposed to binary - interactors. Related to Fig. S1.
963
964
965 **Figure 2. GSK3/AtSK sites in TRAPPII and binary interactions.**
966 **A.** TRAPPII-specific truncations for yeast two-hybrid were based on phylogenetic analysis (Steiner
967 *et al*, 2016). Conserved sequences are depicted in red, intermediate degrees of conservation in
968 orange, and plant-specific sequences are in green. All three GSK3 sites found to be
969 phosphorylated *in vivo* (delineated by a blue rectangle) reside in the plant-specific moiety of
970 TRS120-T2 (green).
971 **B.** GSK3 sites in TRS120-T2. The α-phosphosite of AtTRS120 spans amino acid positions S922
972 and S923, the β-phosphosite amino acids S971-S975 and the γ-phosphosite amino acid residue
973 S1165. The canonical GSK3 consensus sequence is: (pS/pT)*XXX*(S/T), and the β-phosphosite
974 fits this definition (see underlined SXXXS). Even though they are annotated as GSK3 sites in the
975 PPSP (https://www.phosphosite.org) database, the α-phosphosite deviates somewhat with
976 SXXXXS, and the γ-phosphosite deviates completely. Amino acids in red were mutated to A or D
977 via site-directed mutagenesis. Amino acids highlighted in yellow were found to be phosphorylated
978 *in vivo* and these were all serines (see Fig. S2).
979 **C, D.** Mapping of GSK3/AtSK sites on an Alphafold structural prediction (Jumper *et al*, 2021;
980 Varadi *et al*, 2022) of AtTRS120. A lateral view (C) and a frontal perspective (D) are shown. Note
981 that all three GSK3/AtSK sites reside in unstructured, flexible and accessible regions of the
982 protein.
983 **E.** The Arabidopsis TRAPPII complex consists of six shared core subunits (light blue) and three
984 TRAPPII-specific subunits (CLUB/AtTRS130, AtTRS120 and the plant-specific subunit TRIPP),
985 and forms a dimer with plant-specific domains (green) at the predicted dimer interface (Garcia *et*
986 *al*, 2020; Kalde *et al*, 2019). A Rab-GTPase (beige) is shown to bind core-TRAPP subunits at the
987 approximate location of the putative GEF catalytic site, based on yeast models (Cai *et al*, 2008;
988 Thomas *et al*, 2019).
989 **F.** Yeast two-hybrid assays of interactions between BIN2 and TRAPPII truncations (CLUB-C2,
990 CLUB-C3, TRS120-T1, TRS120-T3), as positive controls, fused to the GAL4 DNA-binding domain
991 (DB) and TRS120-T2 truncation and its phosphomutants TRS120-T2 SαD, SβD, SγD, SαβD and
992 SαβγD fused to the GAL4 activation domain (AD). As negative control, the BIN2-DB construct was
993 tested with the empty AD vector. Interactions were verified by pairwise one-on-one mating in four
994 independent replicate experiments; for the control (Co) only one representative example is shown.
995 The panels are from different plates. The results show interactions between BIN2 and AtTRS120-

996 T2 wild-type and phosphovariants; there was, however, no reproducible interaction if all three
997 target sites were phosphomimetic. Related to Fig. S1-S5.
998
999
1000 **Figure 3. *In vitro* AtSK kinase assays with TRS120 as bait.**
1001 **A.** *In vitro* kinase assays using GST:AtSK11 (72 kDa) and GST:TRS120-T2 (100 kDa). The
1002 change of phosphosignal is shown in a representative autoradiograph (upper panel) and the
1003 loaded protein amount in the corresponding CBB (lower panel). Non-phosphorylated variants were
1004 used as negative controls. The means ±SD of phosphosignals were normalized to the protein
1005 amount; nonmutated TRS120-T2 WT is set at 1.0 (right panel); n = 3 independent experiments; *:
1006 P<0.05 paired two-sided student's t-test; TRS120-T2-SαβγA versus TRS120-T2 WT).
1007 **B.** AtTRS120-T2 has highly (red) and moderately (orange) conserved sequences, as well as plant-
1008 specific sequences (green). Three GSK3 sites (referred to as α, β, γ; see Fig. 2B) can be found in
1009 the plant-specific T2 domain.
1010 **C.** Kinase assays were performed *in vitro* with mass-spectrometry readout. One member of each
1011 shaggy-like kinase clade (AtSKs; see Fig. S3A) was used with the TRS120-T2 truncation as
1012 substrate. Dilution series are depicted in different shades of blue. AtSKs in clades I-III differentially
1013 phosphorylate the substrate at three GSK3 consensus sites (with a preference for the γ site) in a
1014 time-dependent and concentration-dependent manner. A clade IV AtSK did not phosphorylate at
1015 all. Samples incubated for 120 min in a kinase buffer without ATP, or samples in which the kinase
1016 was heat inactivated, served as negative controls. The numbers in grey in each plot denote the
1017 number of times the phosphorylation event was seen in the given number of independent
1018 replicates. Note the higher intensity of the TRS120-γ peptide, especially for Clade I/SK11 (1e8 for
1019 TRS120-γ versus 1e6 for TRS120-α and TRS120-β on the Y axis). Related to Fig. S1-S6.
1020
1021
1022 **Figure 4. Role of the TRAPPII complex versus ECHIDNA in hypocotyl/root tradeoffs.**
1023 Seedlings were germinated on ½ MS in the dark (dark) or in dark with -0.4MPa water stress
1024 (darkW). **A.** Col-0 (wild-type). **B.** BR signaling mutant *bin2-3bil1bil2* triple knockout (from Kalbfuß
1025 *et al*, 2022). **C.** *club-2*, a null *trappii* mutant. **D.** *trs120-4*, a null *trappii* allele. **E.** *echidna* null allele,
1026 impaired in TGN structure and function. At least 3 experiments were performed for each line, and
1027 a representative one is shown here on the basis of RQ and *P*-values. **F.** Violin plot for a direct
1028 comparison between *trs120-4* and the corresponding wild-type (Col-0; in the same experiment
1029 and on the same PEG plates) showing that the response to a shift from dark to darkW seen in the

1030 wild-type was not observed in *trs120-4*. **G.** Normalized response quotient RQ_{ratio}. Each replicate
1031 is represented by a dot. Note that the triple *bin2-3bil1bil2* knock out, *trs120-4* and *club-2* had
1032 attenuated responses (magenta arrows). **H.** Volcano plot with the mean RQ_{ratio} depicted on the X
1033 axis and the median *P*-value of the response on the Y axis (negative log scale; a median of all
1034 replicates was used). The area shaded in grey on the red line (green arrow) is where wild-type
1035 ecotypes would theoretically map onto the plot. Mutants in the lower left quadrant (peach shading)
1036 were considered to have a "confused decision phenotype" (see text). *trs120-4* mutants mapped to
1037 the lower left quadrant and qualified as decision mutants on two counts: (i) a consistently opposite
1038 hypocotyl response (red asterisk in D), (ii) failure to adjust the hypocotyl/root ratio to darkW (the
1039 ratio for darkW is the same as for dark in panel D), translating into a non-significant *P*-value for
1040 the ratio response (H). The number (n) of seedlings measured per condition is in grey below the
1041 mean ±SD bar graphs. *P*-values were computed with a two-tailed student's t-test and are
1042 represented as follows: *: P<0.05; **: P<0.01; ***: P<0.001; ****: P<0.0001; *****: P<0.00001.
1043 Mutant alleles and the corresponding ecotypes are described in Table S1. See related Fig. S7.
1044
1045
1046 **Figure 5. Cell elongation in *trappii* hypocotyls under additive stress.**
1047 **A.** Col-0 wild-type.
1048 **B.** *club-2,* null *trappii* allele.
1049 **C.** *trs120-4,* null *trappii* allele.
1050 Seedlings were germinated in the light, or in the dark with (darkW) or without (dark) water stress
1051 (PEG -0.4MPa). The cellular growth parameters width and height were measured based on SEM
1052 images. The cell surface area was calculated as the product of cell width and length. The *trappii*
1053 mutants, *club-2* and *trs120-4*, showed the opposite hypocotyl cell height and cell surface
1054 adaptations to dark-to-darkW conditions (red asterisks in B and C) than the wild-type control.
1055 Representative SEM images of seedlings grown under the specified conditions are shown
1056 (scalebar = 20 µm). The sample size (n) is given as the number of cells/ number of seedlings that
1057 were analyzed in grey below the graph. Shown are means ±SD. *P*-values were computed with a
1058 two-tailed student's t-test and are represented as follows: ***: P<0.001; ****: P<0.0001; *****:
1059 P<0.00001.
1060
1061

1062 **Figure 6. Root meristem properties of *trappii* mutants under single versus additive stress**
1063 **conditions.** Seedlings were grown in the light (orange), dark (black) or dark with -0.4MPa water
1064 stress (darkW; blue).
1065 **A-D.** Col-0 wild-type.
1066 **E-H.** *trs120-4* null mutant.
1067 (A-C) and (E-G) confocal micrographs of mPS-PI stained root tips under different environmental
1068 conditions; black arrows mark the junction between the meristematic and elongation zones.
1069 **D, H.** 10 days after incubation, the cell lengths were measured in single cortex cell files, starting
1070 at the cortex/endodermis initials. The fitted lines were generated with Local Polynomial Regression
1071 Fitting with the 'loess' method in R; grey shading designates the 95 percent confidence interval.
1072 Cell lengths of consecutive cells as a function of cell number from the quiescent centre (QC); the
1073 green arrows point to the steep slope under the dark condition and steeper slope under darkW
1074 condition - the initiation of elongation - in the wild-type (D); magenta arrows point to flatter,
1075 unadjusted slopes under dark versus darkW in *trappii* (*trs120-4*) mutants (H). The sample size (n)
1076 is given as the number of cells/ number of seedlings that were analyzed in panels (D,H). Scale
1077 bar is 50 µm.
1078
1079
1080 **Figure 7. Responses of TRS120 phosphovariants to osmotic or additive stress.**
1081 Phosphovariants of P_{TRS120}::TRS120-GFP (Rybak *et al*, 2014) were in *trs120-4* homozygous
1082 backgrounds with the exception of the TRS120-SαβγD variant in panels A-C, which was in a
1083 hemizygous *trs120-4*/+ background.
1084 **A-C.** Germination of TRS120 phosphovariants under osmotic stress**.** Effect of A) 0 mM, B) 200
1085 mM and C) 400 mM mannitol on seed germination of the TRS120-SαβγA, the TRS120-SαβγD
1086 mutants and the following controls: Col-0 wild-type; the ABA deficient mutant *aba2-1* and the ABA
1087 PP2C co receptor triple knock-out line *hab1-1 abi1-2 pp2ca-1*. The non-phosphorylatable
1088 TRS120-SαβγA mutation increased seed germination on higher mannitol concentrations, whereas
1089 the phosphomimetic TRS120-SαβγD decreased seed germination. Shown are the means ± SD of
1090 three technical replicates. Similar results were obtained in three independent biological replicates.
1091 Stars indicate statistical significance compared to the wild-type Col-0 calculated with a two-tailed
1092 student's t-test (*: P<0.05; **: P<0.01; ***: P<0.001; ****: P<0.0001; *****: P<0.00001). DAS: days
1093 after stratification.
1094 **D-F**. Response quotients (RQ) of A) the hypocotyl, B) the root and C) the hypocotyl/root ratio of
1095 the non-phosphorylatable TRS120-SαβγA and the phosphomimetic TRS120-SαβγD mutants for

1096 dark-to-dark with water stress (-0.4MPa, darkW) adaptation. The divergent hypocotyl and root
1097 responses of TRS120-SαβγA and TRS120-SαβγD mutants resulted in a strong hypocotyl/root
1098 ratio phenotype under darkW conditions compared to the TRS120-WT control. TRS120-SαβγA
1099 showed an enhanced ratio adaption, whereas TRS120-SαβγD mutants had an attenuated ratio
1100 response. RQ response quotients are normalized to the rescue mutant TRS120-WT
1101 (P_{TRS120}::TRS120-GFP in *trs120-4/trs120-4*). A value of 1 (vertical red line) corresponds to an
1102 identical adaptation to darkW conditions as the rescue mutant. Dots represent biological
1103 replicates, of which there were a total of four primary transformants per line. Mean RQ values are
1104 given on the right.
1105
1106
1107 **Figure 8. Flow diagram suggesting how BIN2 might mediate plant adaptive responses by**
1108 **phosphorylating the TRAPPII complex.**
1109 Shaggy-like kinases such as BIN2 integrate a vast number of signaling pathways and, together
1110 with receptor complexes at the cell surface, comprise a surveillance system fine-tuned to both
1111 biotic and abiotic cues (Lv & Li, 2020; Planas-Riverola *et al*, 2019; Youn & Kim, 2015; Li *et al*,
1112 2021; Song *et al*, 2023). BIN2 resides at the plasma membrane and in the cytosol and TRAPPII
1113 resides at the cytosol and in the TGN (Qi *et al*, 2011; Naramoto *et al*, 2014; Rybak *et al*, 2014;
1114 Ravikumar *et al*, 2018). We propose that, in the cytosol, the BIN2-TRAPPII interaction serves in
1115 the relay of information from the PM to the TGN. As an early endosome, the TGN is a central hub
1116 in the flow of information to and from the cell surface. It is also intimately connected to the late
1117 endosome (or the pre-vacuolar compartment) and to the Golgi. Thus, the AtSK-TRAPPII
1118 interaction would integrate all levels of cellular organization. We posit that signal integration and
1119 decision-making occur at the AtSK-TRAPPII interface and that, downstream of TRAPPII, Rab
1120 GTPase cascades are implicated in implementing decisions reached at the AtSK-TRAPPII
1121 module.
1122 In the lower panel we show one example of an adaptive growth decision in 10-day-old seedlings
1123 (Col-0 wild-type). Bar plots depict hypocotyl (green) versus root (beige-brown) lengths. Light: light
1124 grown seedling with a short hypocotyl and a long root. Dark: a seedling germinated in the dark
1125 with a long hypocotyl and a short root. DarkW: Water deprivation in the dark; the hypocotyl is
1126 shorter and the root longer than under dark conditions. The dotted green arrow (dark, darkW)
1127 represents the incentive for hypocotyl elongation in search of light and the brown arrow (darkW)
1128 the incentive for root growth in search of water. Thus, darkW is a “conflict of interest” scenario in
1129 which hypocotyl and root growth have competing interests (Kalbfuß *et al*, 2022). Figure created
1130 with BioRender.

1131 **SUPPORTING INFORMATION**

1132

1133 **Figure S1.** Selected brassinosteroid signaling components in CLUB:GFP IP-MS.

1134 **Figure S2.** Fragment ion mass spectra of AtTRS120 phosphopeptides found in TRS120:GFP
1135 IP-MS.

1136 **Figure S3.** Fragment ion mass spectra of AtSK/GSK3 kinases found in TRS120:GFP IP-MS.

1137 **Figure S4.** BIN2 phosphorylates TRS120 preferentially at the Sγ site.

1138 **Figure S5.** Pharmacological inhibition of TRAPPII phosphorylation by AtSKs *in vivo.*

1139 **Figure S6.** Cytokinesis and protein sorting in *bin2-1.*

1140 **Figure S7.** Response to additive stress: response quotients and volcano plots.

1141 **Figure S8.** Light responses in *bin2*, *trappii* and *echidna* mutants.

1142 **Figure S9.** Characterization of TRS120:GFP phosphovariants.

1143 **Figure S10.** Localization of TRS120:GFP phosphovariants.

1144 **Figure S11.** The etiolation response in TRS120 phosphovariants.

1145 **Figure S12.** Role of TRS120 phosphorylation status on adaptive growth responses under
1146 additive stress conditions.

1147 **Table S1.** Mutant lines used in this study.

1148 **Table S2.** Selected brassinosteroid signaling proteins in the CLUB interactome.

1149 **Supporting Methods.**

1150

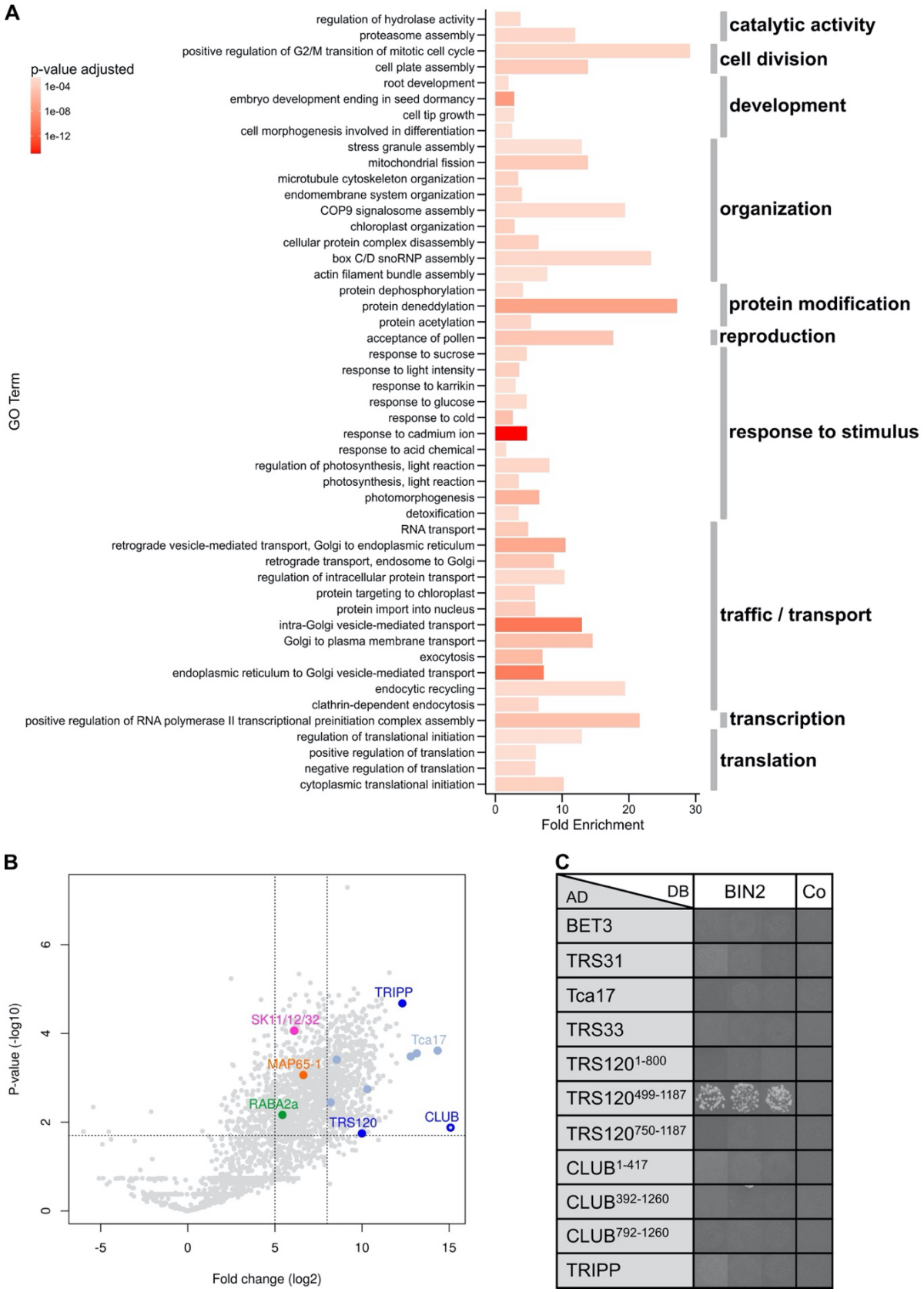

Figure 1. The TRAPPII interactome.

A. Gene ontology (GO) term enrichment analysis of the TRAPPII interactome. Depicted are fold enrichments

of GO terms of level 0 as bar plots colored by significance level. The data are derived from an analysis of IP-MS from inflorescences with the TRAPPII-specific subunit CLUB-GFP as bait (see Fig. 1B; Kalde *et al*, 2019). Terms are grouped by manually annotated super-categories. Metabolic processes were excluded for simplification. Note that the super categories organization (9) and traffic/transport (12) make up the majority of GO terms (21/49) and that response to stimulus (11) comprises the second largest category. Cutoffs were set at 1.5 for fold-change and 0.003 for the *P*-value, which was adjusted for the false discovery rate.
B. IP-MS with the TRAPPII-specific subunit CLUB-GFP as bait (Kalde *et al*, 2019). Inflorescences were used. Each protein was present in all three biological replicates. The ratio (or fold-change) was calculated for each protein as the average intensity of the signal in the experiment divided by its average intensity in the soluble GFP empty vector control. The *P*-value (depicted along a negative log10 scale) is plotted against the signal ratio. Dotted grey lines represent cutoffs: *P*-value < 0.02 and Ratio > 8 or > 5. Note that TRAPPII subunits (light blue for core TRAPP; dark blue for TRAPPII-specific subunits; the AtTRS130/CLUB-GFP TRAPPII-specific bait is depicted as an open circle) are in the upper right field, indicating high abundance and good reproducibility. AtSKs (magenta), MAP65-1 (orange) and Rab A2a GTPase (green) are all in the upper middle field; these may be transient interactors of TRAPPII. Note that AtSKs (AtSK11/12/32) are more significant than validated interactors such as MAP65 and RabA2a (Kalde *et al*, 2019; Steiner *et al*, 2016).
C. Yeast two-hybrid assays of interactions between BIN2 and TRAPPII subunits. BIN2 was fused to the GAL4 DNA-binding domain (DB) and TRAPPII subunits and truncations thereof (CLUB$^{1-417}$, CLUB$^{392-1260}$, CLUB$^{792-1260}$, TRS120$^{1-800}$, TRS120$^{499-1187}$ and TRS120$^{750-1187}$; referred to below as CLUB-C1, -C2, -C3 and TRS120-T1, -T2, -T3) to the GAL4 activation domain (AD). As negative control, the BIN2-DB construct was tested with the empty AD vector. Interactions were verified by pairwise one-on-one mating in four independent replicate experiments. The panels are from different plates. The results show interactions between BIN2 and AtTRS120$^{499-1187}$ wild-type. BIN2 bound specifically to the TRAPPII subunit TRS120 (TRS120$^{499-1187}$ / T2 truncation) and not with other TRAPPII subunits or truncations. In a total of > 2400 pairwise tests, BIN2 was the only kinase we found that interacted with a TRAPP subunit. The Y2H did not detect AtTRS130/CLUB-BIN2 interaction shown in Fig. 1B, which shows co-purified proteins that can include indirect - as opposed to binary - interactors. Related to Fig. S1.

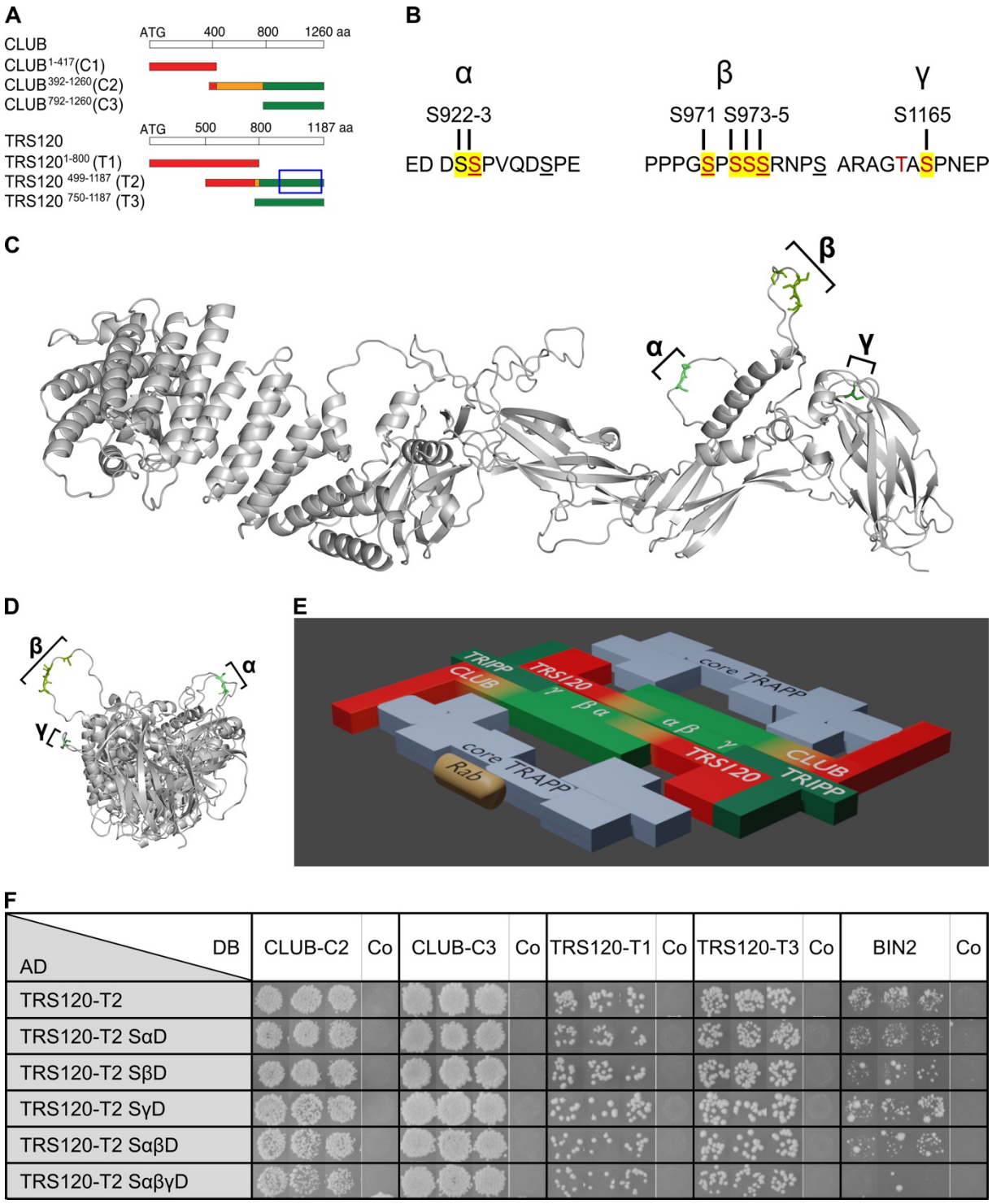

Figure 2. GSK3/AtSK sites in TRAPPII and binary interactions.

A. TRAPPII-specific truncations for yeast two-hybrid were based on phylogenetic analysis (Steiner *et al*, 2016). Conserved sequences are depicted in red, intermediate degrees of conservation in orange, and plant-specific sequences are in green. All three GSK3 sites found to be phosphorylated *in vivo* (delineated by a blue rectangle) reside in the plant-specific moiety of TRS120-T2 (green).

B. GSK3 sites in TRS120-T2. The α-phosphosite of AtTRS120 spans amino acid positions S922 and S923, the β-phosphosite amino acids S971-S975 and the γ-phosphosite amino acid residue S1165. The canonical GSK3 consensus sequence is: (pS/pT)*XXX*(S/T), and the β-phosphosite fits this definition (see underlined

SXXXS). Even though they are annotated as GSK3 sites in the PPSP (https://www.phosphosite.org) database, the α-phosphosite deviates somewhat with SXXXXS, and the γ-phosphosite deviates completely. Amino acids in red were mutated to A or D via site-directed mutagenesis. Amino acids highlighted in yellow were found to be phosphorylated *in vivo* and these were all serines (see Fig. S2).
C, D. Mapping of GSK3/AtSK sites on an Alphafold structural prediction (Jumper *et al*, 2021; Varadi *et al*, 2022) of AtTRS120. A lateral view (C) and a frontal perspective (D) are shown. Note that all three GSK3/AtSK sites reside in unstructured, flexible and accessible regions of the protein.
E. The Arabidopsis TRAPPII complex consists of six shared core subunits (light blue) and three TRAPPII-specific subunits (CLUB/AtTRS130, AtTRS120 and the plant-specific subunit TRIPP), and forms a dimer with plant-specific domains (green) at the predicted dimer interface (Garcia *et al*, 2020; Kalde *et al*, 2019). A Rab-GTPase (beige) is shown to bind core-TRAPP subunits at the approximate location of the putative GEF catalytic site, based on yeast models (Cai *et al*, 2008; Thomas *et al*, 2019).
F. Yeast two-hybrid assays of interactions between BIN2 and TRAPPII truncations (CLUB-C2, CLUB-C3, TRS120-T1, TRS120-T3), as positive controls, fused to the GAL4 DNA-binding domain (DB) and TRS120-T2 truncation and its phosphomutants TRS120-T2 SαD, SβD, SγD, SαβD and SαβγD fused to the GAL4 activation domain (AD). As negative control, the BIN2-DB construct was tested with the empty AD vector. Interactions were verified by pairwise one-on-one mating in four independent replicate experiments; for the control (Co) only one representative example is shown. The panels are from different plates. The results show interactions between BIN2 and AtTRS120-T2 wild-type and phosphovariants; there was, however, no reproducible interaction if all three target sites were phosphomimetic. Related to Fig. S1-S5.

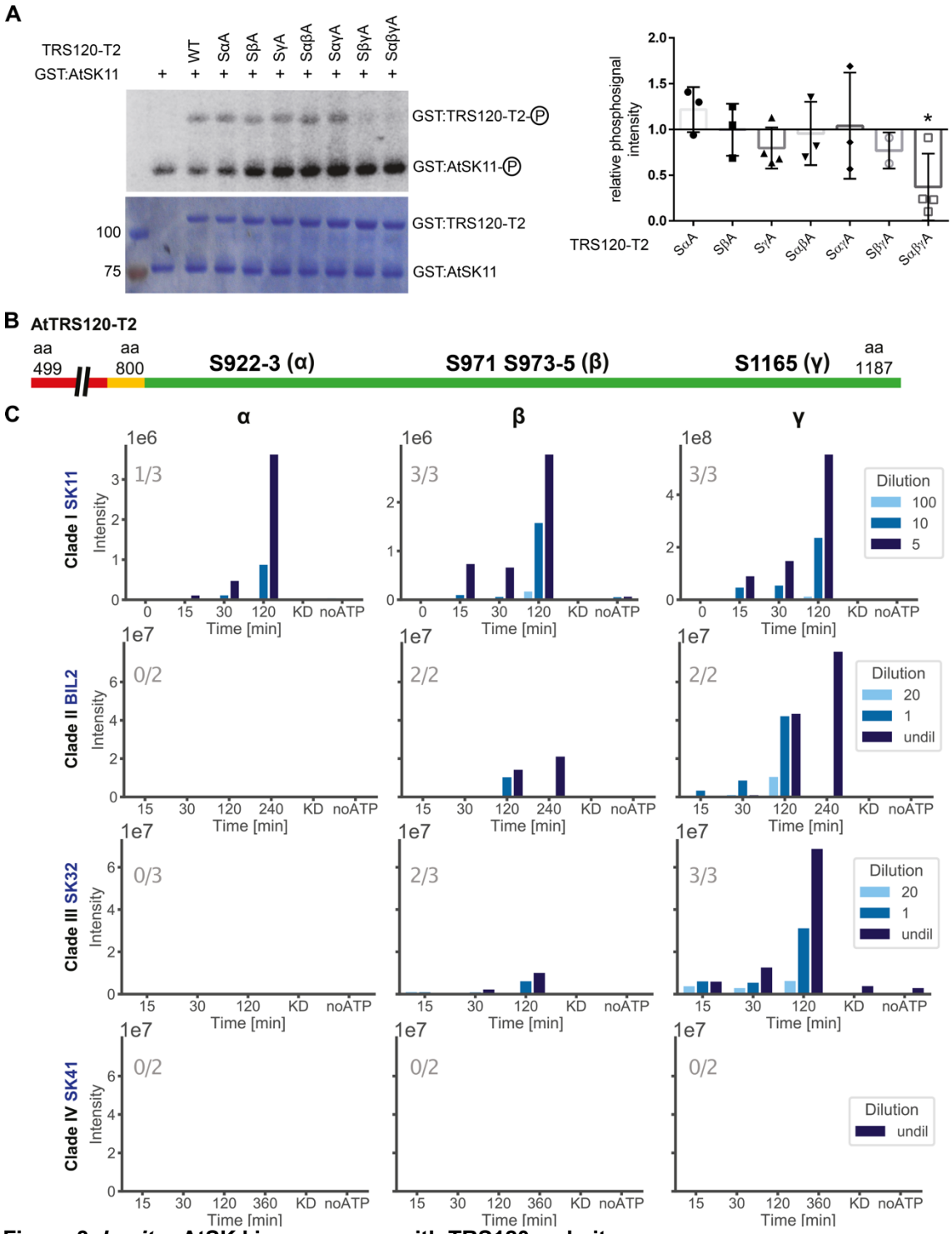

Figure 3. *In vitro* AtSK kinase assays with TRS120 as bait.

A. *In vitro* kinase assays using GST:AtSK11 (72 kDa) and GST:TRS120-T2 (100 kDa). The change of phosphosignal is shown in a representative autoradiograph (upper panel) and the loaded protein amount in the corresponding CBB (lower panel). Non-phosphorylated variants were used as negative controls. The means ±SD of phosphosignals were normalized to the protein amount; nonmutated TRS120-T2 WT is set at 1.0 (right panel); n = 3 independent experiments; *: P<0.05 paired two-sided student's t-test; TRS120-T2-SαβγA versus TRS120-T2 WT).

B. AtTRS120-T2 has highly (red) and moderately (orange) conserved sequences, as well as plant-specific sequences (green). Three GSK3 sites (referred to as α, β, γ; see Fig. 2B) can be found in the plant-specific T2 domain.
C. Kinase assays were performed *in vitro* with mass-spectrometry readout. One member of each shaggy-like kinase clade (AtSKs; see Fig. S3A) was used with the TRS120-T2 truncation as substrate. Dilution series are depicted in different shades of blue. AtSKs in clades I-III differentially phosphorylate the substrate at three GSK3 consensus sites (with a preference for the γ site) in a time-dependent and concentration-dependent manner. A clade IV AtSK did not phosphorylate at all. Samples incubated for 120 min in a kinase buffer without ATP, or samples in which the kinase was heat inactivated, served as negative controls. The numbers in grey in each plot denote the number of times the phosphorylation event was seen in the given number of independent replicates. Note the higher intensity of the TRS120-γ peptide, especially for Clade I/SK11 (1e8 for TRS120-γ versus 1e6 for TRS120-α and TRS120-β on the Y axis). Related to Fig. S1-S6.

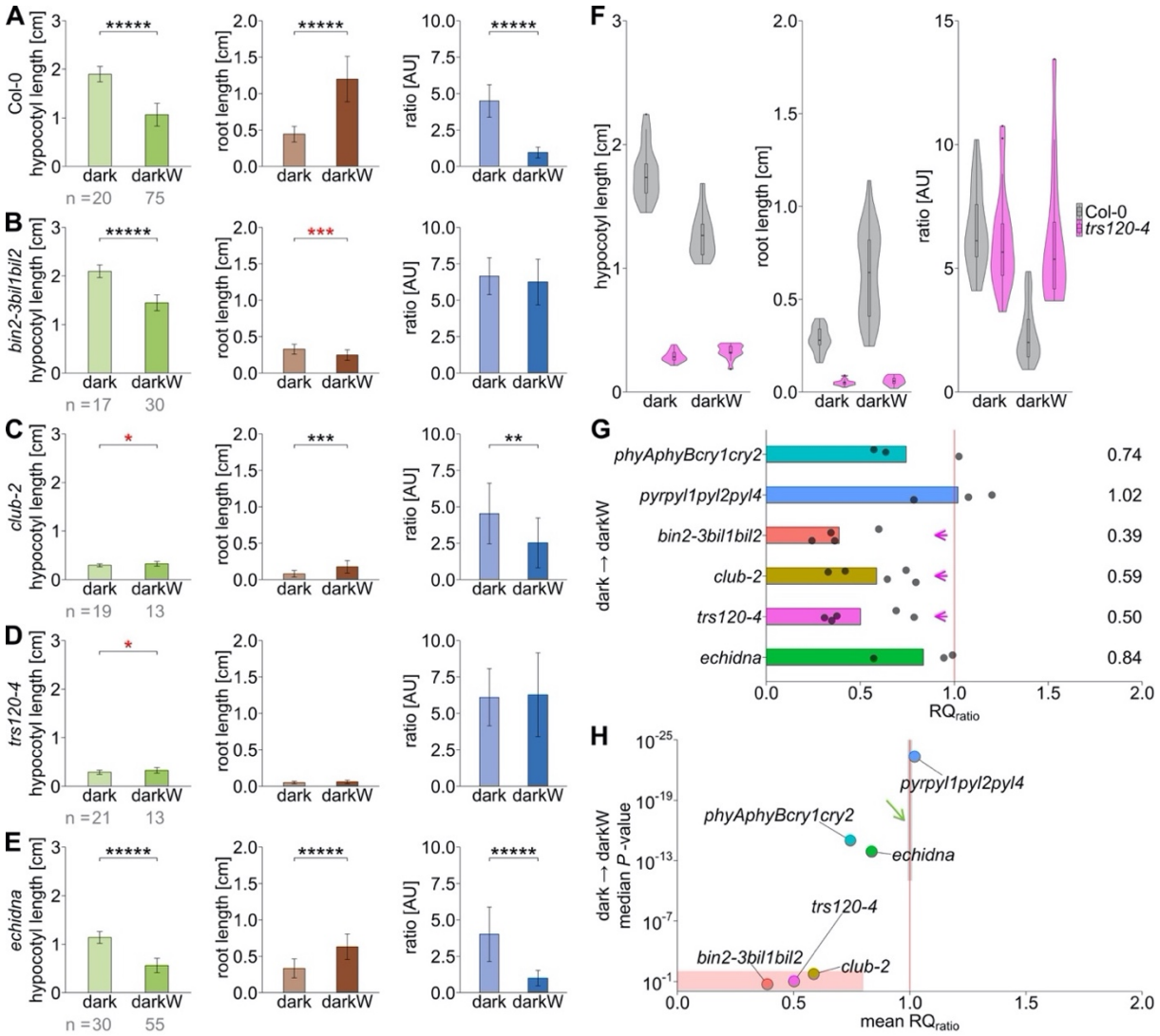

Figure 4. Role of the TRAPPII complex versus ECHIDNA in hypocotyl/root tradeoffs.
Seedlings were germinated on ½ MS in the dark (dark) or in dark with -0.4MPa water stress (darkW). **A.** Col-0 (wild-type). **B.** BR signaling mutant *bin2-3bil1bil2* triple knockout (from Kalbfuß *et al*, 2022). **C.** *club-2*, a null *trappii* mutant. **D.** *trs120-4*, a null *trappii* allele. **E.** *echidna* null allele, impaired in TGN structure and function. At least 3 experiments were performed for each line, and a representative one is shown here on the basis of RQ and *P*-values. **F.** Violin plot for a direct comparison between *trs120-4* and the corresponding wild-type (Col-0; in the same experiment and on the same PEG plates) showing that the response to a shift from dark to darkW seen in the wild-type was not observed in *trs120-4*. **G.** Normalized response quotient RQ_{ratio}. Each replicate is represented by a dot. Note that the triple *bin2-3bil1bil2* knock out, *trs120-4* and *club-2* had attenuated responses (magenta arrows). **H.** Volcano plot with the mean RQ_{ratio} depicted on the X axis and the median *P*-value of the response on the Y axis (negative log scale; a median of all replicates was used). The area shaded in grey on the red line (green arrow) is where wild-type ecotypes would theoretically map onto the plot. Mutants in the lower left quadrant (peach shading) were considered to have a "confused decision phenotype" (see text). *trs120-4* mutants mapped to the lower left quadrant and qualified as decision mutants on two counts: (i) a consistently opposite hypocotyl response (red asterisk in D), (ii) failure to adjust the hypocotyl/root ratio to darkW (the ratio for darkW is the same as for dark in panel D), translating into a non-significant *P*-value for the ratio response (H). The number (n) of seedlings measured per condition is in grey below the mean ±SD bar graphs. *P*-values were computed with a two-tailed student's t-test and are represented as follows: *: P<0.05; **: P<0.01; ***: P<0.001; ****: P<0.0001; *****: P<0.00001. Mutant alleles and the corresponding ecotypes are described in Table S1. See related Fig. S7.

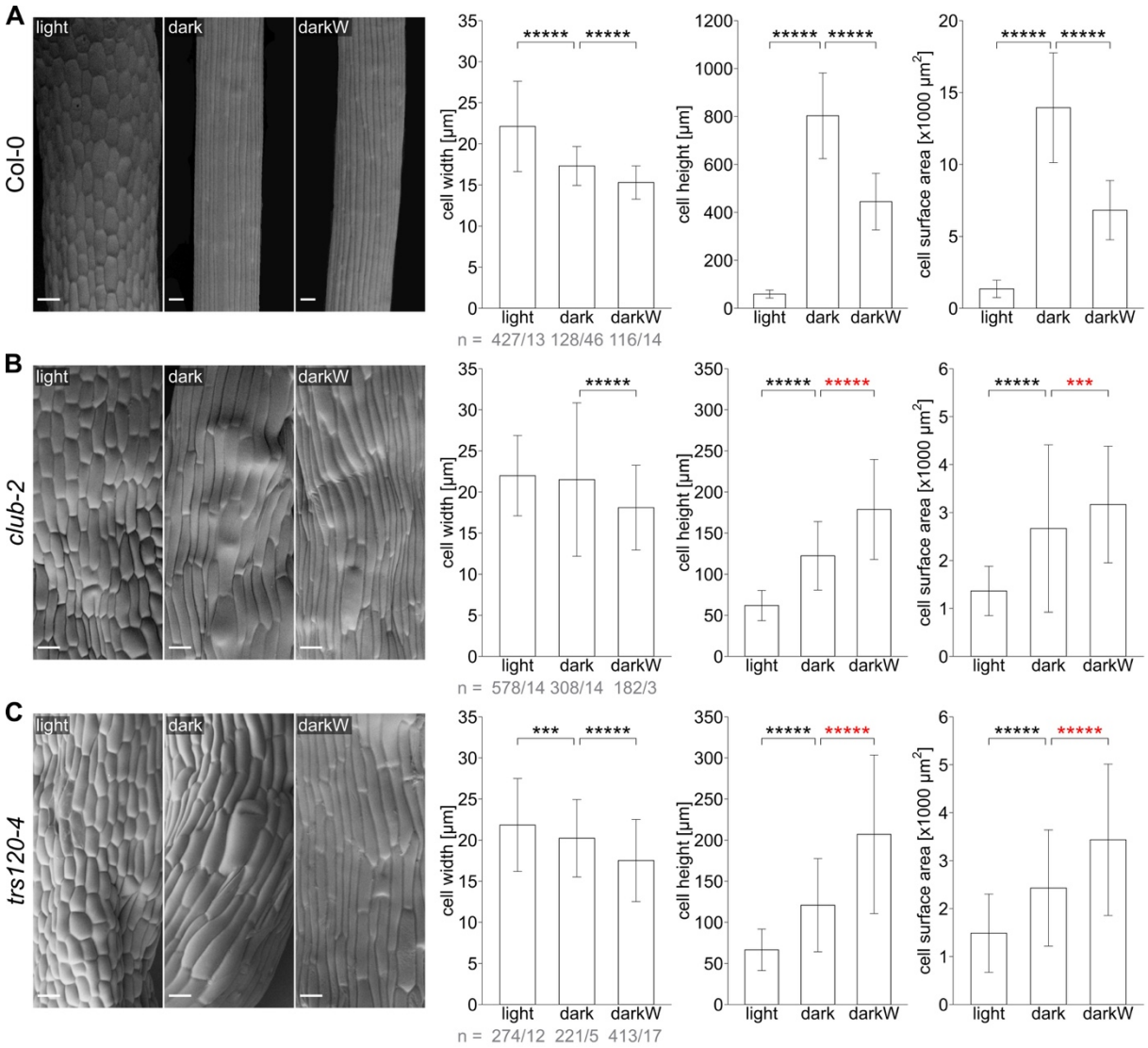

Figure 5. Cell elongation in *trappii* hypocotyls under additive stress.

A. Col-0 wild-type.

B. *club-2,* null *trappii* allele.

C. *trs120-4,* null *trappii* allele.

Seedlings were germinated in the light, or in the dark with (darkW) or without (dark) water stress (PEG - 0.4MPa). The cellular growth parameters width and height were measured based on SEM images. The cell surface area was calculated as the product of cell width and heigth. The *trappii* mutants, *club-2* and *trs120-4*, showed the opposite hypocotyl cell height and cell surface adaptations to dark-to-darkW conditions (red asterisks in B and C) than the wild-type control. Representative SEM images of seedlings grown under the specified conditions are shown (scalebar = 20 µm). The sample size (n) is given as the number of cells/ number of seedlings that were analyzed in grey below the graph. Shown are means ±SD. *P*-values were computed with a two-tailed student's t-test and are represented as follows: ***: P<0.001; ****: P<0.0001; *****: P<0.00001.

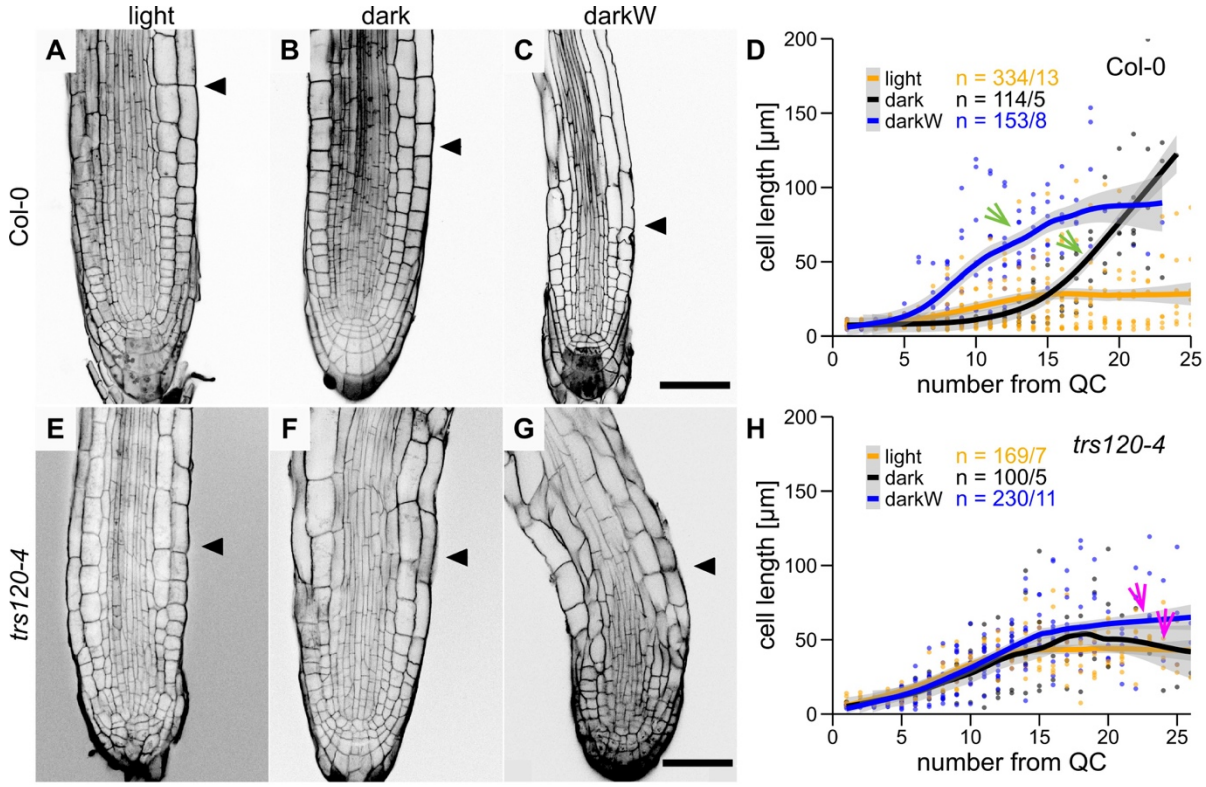

Figure 6. Root meristem properties of *trappii* mutants under single versus additive stress conditions. Seedlings were grown in the light (orange), dark (black) or dark with -0.4MPa water stress (darkW; blue).

A-D. Col-0 wild-type.

E-H. *trs120-4* null mutant.

(A-C) and (E-G) confocal micrographs of mPS-PI stained root tips under different environmental conditions; black arrows mark the junction between the meristematic and elongation zones.

D, H. 10 days after incubation, the cell lengths were measured in single cortex cell files, starting at the cortex/endodermis initials. The fitted lines were generated with Local Polynomial Regression Fitting with the 'loess' method in R; grey shading designates the 95 percent confidence interval. Cell lengths of consecutive cells as a function of cell number from the quiescent centre (QC); the green arrows point to the steep slope under the dark condition and steeper slope under darkW condition - the initiation of elongation - in the wild-type (D); magenta arrows point to flatter, unadjusted slopes under dark versus darkW in *trappii* (*trs120-4*) mutants (H). The sample size (n) is given as the number of cells/ number of seedlings that were analyzed in panels (D,H). Scale bar is 50 µm.

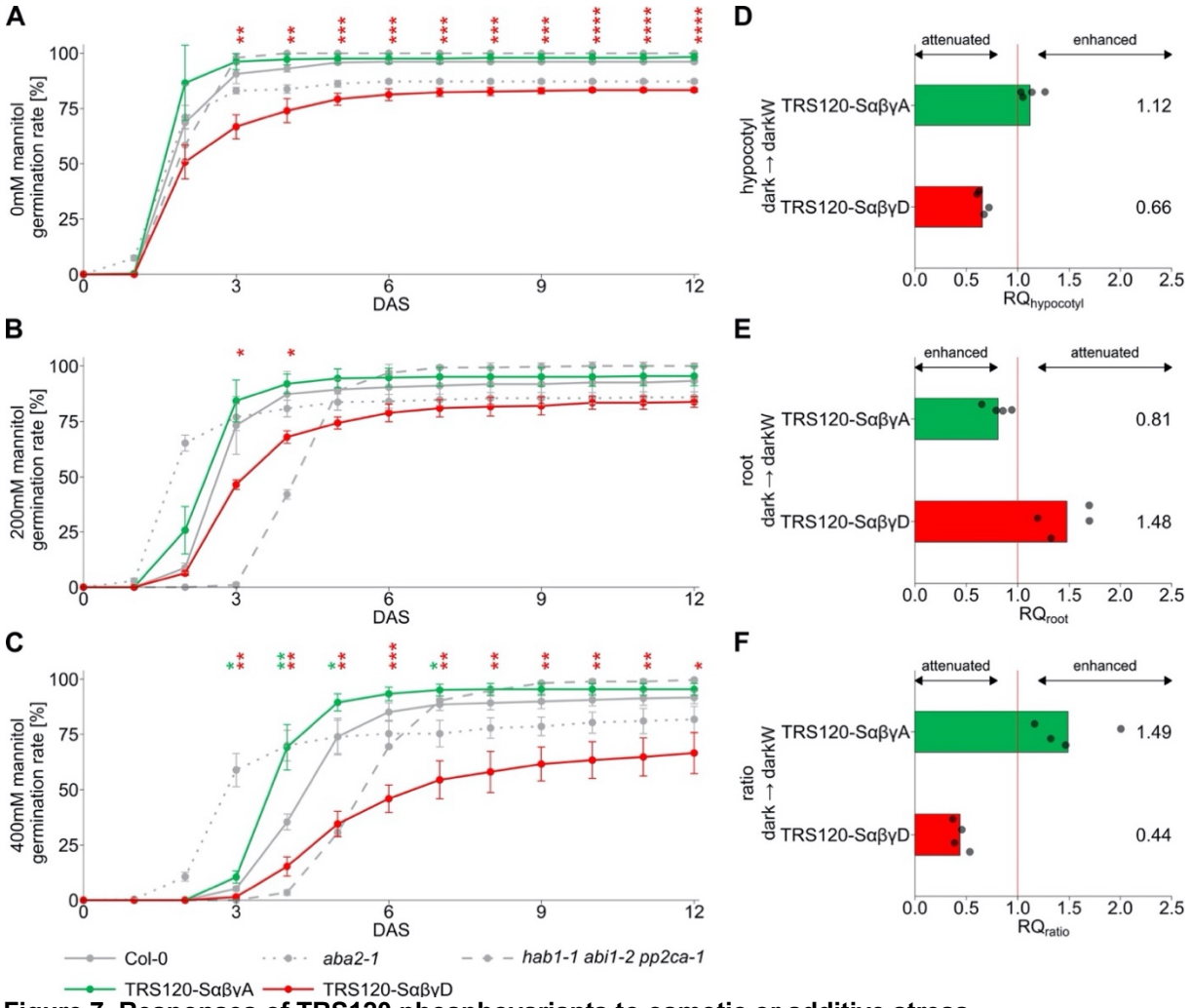

Figure 7. Responses of TRS120 phosphovariants to osmotic or additive stress.

Phosphovariants of P_{TRS120}::TRS120-GFP (Rybak *et al*, 2014) were in *trs120-4* homozygous backgrounds with the exception of the TRS120-SαβγD variant in panels A-C, which was in a hemizygous *trs120-4*/+ background.

A-C. Germination of TRS120 phosphovariants under osmotic stress**.** Effect of A) 0 mM, B) 200 mM and C) 400 mM mannitol on seed germination of the TRS120-SαβγA, the TRS120-SαβγD mutants and the following controls: Col-0 wild-type; the ABA deficient mutant *aba2-1* and the ABA PP2C co receptor triple knock-out line *hab1-1 abi1-2 pp2ca-1*. The non-phosphorylatable TRS120-SαβγA mutation increased seed germination on higher mannitol concentrations, whereas the phosphomimetic TRS120-SαβγD decreased seed germination. Shown are the means ± SD of three technical replicates. Similar results were obtained in three independent biological replicates. Stars indicate statistical significance compared to the wild-type Col-0 calculated with a two-tailed student's t-test (*: P<0.05; **: P<0.01; ***: P<0.001; ****: P<0.0001; *****: P<0.00001). DAS: days after stratification.

D-F. Response quotients (RQ) of A) the hypocotyl, B) the root and C) the hypocotyl/root ratio of the non-phosphorylatable TRS120-SαβγA and the phosphomimetic TRS120-SαβγD mutants for dark-to-dark with water stress (-0.4MPa, darkW) adaptation. The divergent hypocotyl and root responses of TRS120-SαβγA and TRS120-SαβγD mutants resulted in a strong hypocotyl/root ratio phenotype under darkW conditions compared to the TRS120-WT control. TRS120-SαβγA showed an enhanced ratio adaption, whereas TRS120-SαβγD mutants had an attenuated ratio response. RQ response quotients are normalized to the rescue mutant TRS120-WT (P_{TRS120}::TRS120-GFP in *trs120-4/trs120-4*). A value of 1 (vertical red line) corresponds to an identical adaptation to darkW conditions as the rescue mutant. Dots represent biological replicates, of which there were a total of four primary transformants per line. Mean RQ values are given on the right.

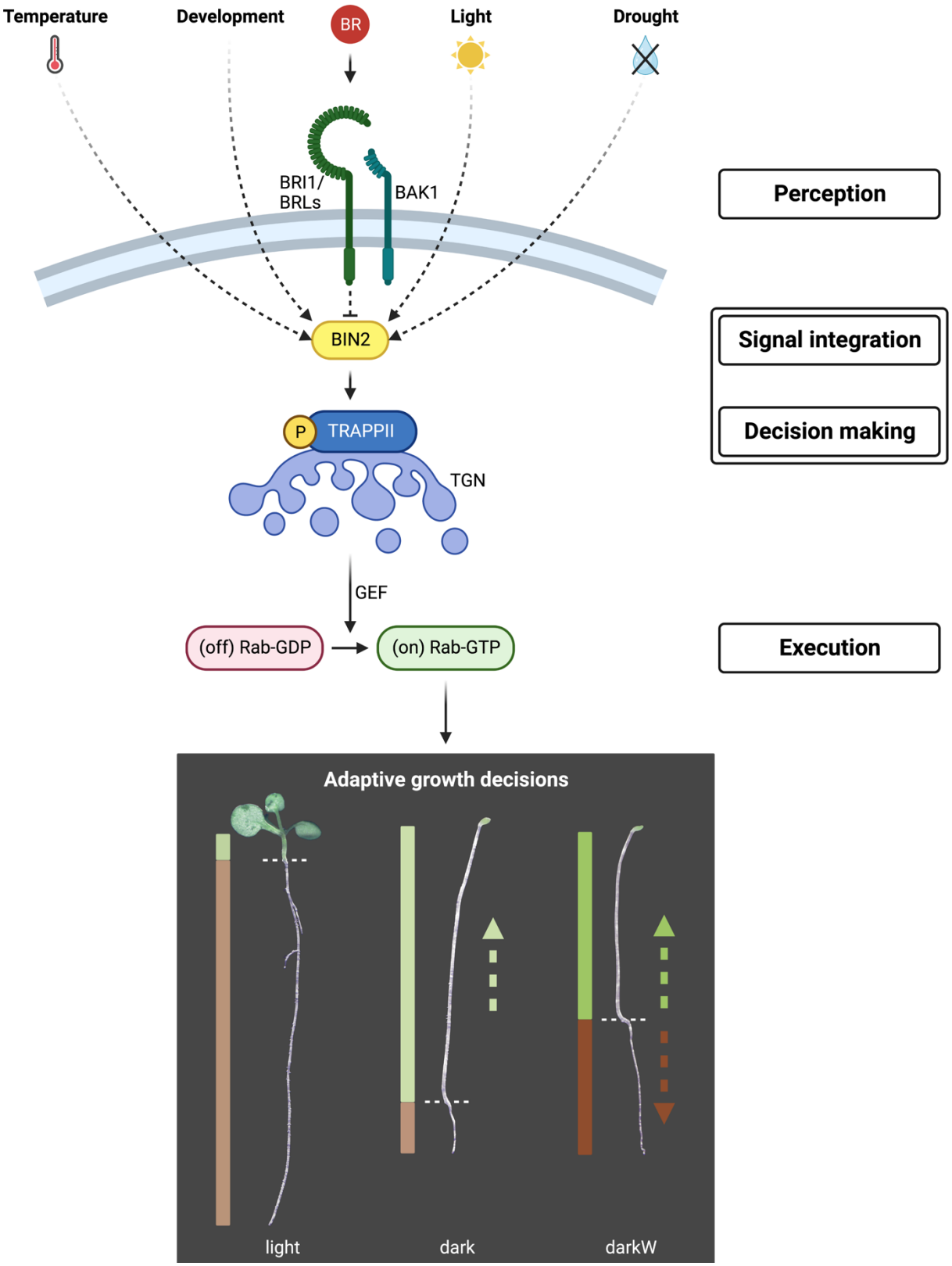

Figure 8. Flow diagram suggesting how BIN2 might mediate plant adaptive responses by phosphorylating the TRAPPII complex.
Shaggy-like kinases such as BIN2 integrate a vast number of signaling pathways and, together with receptor complexes at the cell surface, comprise a surveillance system fine-tuned to both biotic and abiotic cues (Lv

& Li, 2020; Planas-Riverola *et al*, 2019; Youn & Kim, 2015; Li *et al*, 2021; Song *et al*, 2023). BIN2 resides at the plasma membrane and in the cytosol and TRAPPII resides at the cytosol and in the TGN (Qi *et al*, 2011; Naramoto *et al*, 2014; Rybak *et al*, 2014; Ravikumar *et al*, 2018). We propose that, in the cytosol, the BIN2-TRAPPII interaction serves in the relay of information from the PM to the TGN. As an early endosome, the TGN is a central hub in the flow of information to and from the cell surface. It is also intimately connected to the late endosome (or the pre-vacuolar compartment) and to the Golgi. Thus, the AtSK-TRAPPII interaction would integrate all levels of cellular organization. We posit that signal integration and decision-making occur at the AtSK-TRAPPII interface and that, downstream of TRAPPII, Rab GTPase cascades are implicated in implementing decisions reached at the AtSK-TRAPPII module.
In the lower panel we show one example of an adaptive growth decision in 10-day-old seedlings (Col-0 wild-type). Bar plots depict hypocotyl (green) versus root (beige-brown) lengths. Light: light grown seedling with a short hypocotyl and a long root. Dark: a seedling germinated in the dark with a long hypocotyl and a short root. DarkW: Water deprivation in the dark; the hypocotyl is shorter and the root longer than under dark conditions. The dotted green arrow (dark, darkW) represents the incentive for hypocotyl elongation in search of light and the brown arrow (darkW) the incentive for root growth in search of water. Thus, darkW is a “conflict of interest” scenario in which hypocotyl and root growth have competing interests (Kalbfuß *et al*, 2022). Figure created with BioRender.